CHALMERS

Sensor calibration for autonomous mine vehicles

Calibration of laser scanners and hinge angle sensor

Master of Science Thesis

MAGNUS OLOFSSON

Department of Applied Information Technology
CHALMERS UNIVERSITY OF TECHNOLOGY
Göteborg, Sweden, 2011
ISSN 1651-4769
Report No. 2011:031

Sensor calibration for autonomous mine vehicles

Calibration of laser scanners and hinge angle sensor

MAGNUS OLOFSSON

Technical report no 2011:031
Department of Applied Information Technology
Chalmers University of Technology
SE-412 96 Göteborg
Sweden
Telephone + 46 (0)31-772 1000

Cover:
An autonomous ST14 LHD (Load-Haul-Dumper) from Atlas Copco.

Göteborg, Sweden 2011

Sensor calibration for autonomous mine vehicles

Calibration of laser scanners and hinge angle sensor

MAGNUS OLOFSSON
Department of Applied Information Technology
Chalmers University of Technology

Summary

Atlas Copco has delivered mining products since the last century and in 2007 they introduced an autonomous centre articulated LHD (Load-Haul-Dumper). LHD:s are used in most underground mines for transport of ore and the idea of an autonomous

LHD was to improve safety, efficiency and productivity in underground mines. The autonomous LHD contains a number of sensors including an odometer, a hinge angle sensor in the articulation joint, a gyro and two laser scanners needed for autonomous operation. All of them need to be calibrated because of pose errors from high tolerances in the machine construction.

In this thesis a method for calibrating the angular offset of the hinge angle sensor and another method for calibrating the angular offsets of the two laser scanners using data from the already existing sensors are presented. The hinge angle method relies on the gyro, the odometer and a kinematic model of a centre articulated vehicle to estimate the offset. For calibration of the laser scanners the offsets are augmented on to the states in the state space model used for positioning of the LHD. The augmented state is then estimated using a combination of an Extended Kalman filter and an Unscented Kalman filter in a SLAM algorithm that uses the kinematic model and the laser measurements.

Experiments in simulated and real environments have shown that the hinge angle sensor estimates the angular offset to within 0.3^{o}. Tests of the laser scanner calibration method have shown that it estimates the angular offset to within 0.5^{o}. The methods run offline, are easy to operate and require that the operator drives at least 50 m in a straight mine drift at 2.5 m/s to collect enough data.

The report is written in English.

Keywords: calibration, offset, LHD, centre articulated, laser scanner, hinge angle, SLAM, Kalman filter.

Acknowledgements

First of all I want to thank my supervisor Johan Larsson at the Automation department of Atlas Copco for his guidance, support and encouragement. I also want to thank Jörgen Appelgren, manager of the Automation department, for giving me the opportunity to work at the department. Many thanks to my girlfriend Sandra Trygg who has put up with all my work and travelling. Last of all I want to thank my mother Katarina Olofsson and Björn Edling for allowing me to stay at their house and borrow their car under some periods of the thesis.

Contents

1 INTRODUCTION 1

1.1 History 1

1.2 System overview 1

1.3 Objective 2

1.4 Contribution 2

1.5 Report structure 2

2 REQUIREMENTS AND APPROACH 3

2.1 Hinge angle offset 3

2.2 Laser offsets 4

3 THEORY AND METHODS 4

3.1 Kinematic model 5

3.2 Sensors 6
3.2.1 IMU Navigation02 7
3.2.2 Odometer 8
3.2.3 Hinge angle sensor 8
3.2.4 SICK Laser scanner 9

3.3 Hinge angle offset 9
3.3.1 Estimation of the hinge angle offset γ_o 9
3.3.2 Estimation of gyro bias 11
3.3.3 Error propagation 12
3.3.4 Measurement statistics 13

3.4 Laser scanners angular offset 15
3.4.1 Creating and evaluating the map 15
3.4.2 State estimation using nonlinear Kalman filter 15
3.4.3 State augmentation of laser offsets 17
3.4.4 SLAM 19

3.5 Implementation 21

4 ERROR PROPAGATION IN THE HINGE ANGLE METHOD 21

4.1 Analysis setup 21

4.2 Results 22

4.3 Discussion 24

5 HINGE ANGLE EXPERIMENTS 25

5.1 Experiment setup 25

5.2 Results **27**
5.2.1 Driving straight 27
5.2.2 Small turning 28
5.2.3 Increased turning and deadband 29

5.3 Discussion **30**

6 REQUIRED LASER OFFSET ACCURACY **32**

6.1 Analysis setup **32**

6.2 Results **32**

6.3 Discussion **34**

7 ACCURACY OF THE LASER OFFSET ESTIMATION **35**

7.1 Test setup **35**

7.2 Results **36**
7.2.1 Driving straight in a normal mine drift 36
7.2.2 Turning in a normal mine drift 38
7.2.3 Driving in a straight wide mine drift 41

7.3 Discussion **42**

8 CONCLUSION **43**

9 REFERENCES **44**

10 APPENDIX A **45**

10.1 Only using hinge angle measurements **45**

10.2 Gyro ideas **46**

11 APPENDIX B **46**

List of abbreviations

AKF	Augmented Kalman Filter
EKF	Extended Kalman Filter
UKF	Unscented Kalman Filter
LHD	Load Haul Dump machine
SLAM	Simultaneous Localization and Mapping
IMU	Inertial Measurement Unit

1 Introduction

1.1 History

The mining industry is a dangerous workplace, especially underground mining. During the last decades mining companies have tried to improve efficiency, productivity and safety. Atlas Copco AB started out in 1873 as a railway company but turned into air compressors and air tools in the end of the 19th century. Today they are in a number of markets and at the beginning of the 20th century they started producing air driven rock drills to the mining industry. The development has moved on and today they produce a number of mining products including the centre articulated LHD (Load-Haul- Dump) Scooptram ST14 for loading, hauling and dumping materials in underground mines.

All LHD:s have traditionally been manually driven by an operator placed in the machine. But for some years ago solutions began to be used where the LHD was remote controlled and teleoperated from a control room (Hainsworth 2001). With teleoperation the operator was removed from the dangerous mine, but teleoperation includes delays and the cameras restrict the view for the operator which decreases the productivity (Larsson, Broxvall & Saffiotti 2010). To solve the problems related to teleoperation and also remove the need of a operator to each LHD autonomous systems have been developed and are commercially available, see (Automine 2011), (Scooptram Automation 2011) and (MINEGEM 2011). Atlas Copco's Scooptram Automation includes both teleoperation and autonomous operation.

1.2 System overview

Atlas Copco's autonomous system works using the principle Teaching, Route profiling and Playback. First the LHD is driven manually along the route it should operate on and all sensor data are logged. During route profiling data are converted to a number of grid maps (Marshall, Barfoot, & Larsson 2008) and a route profile containing waypoints, desired speeds and pause points for loading and dumping.

During playback the route is followed with help of the sensors. Data from a hinge angle sensor in the articulation joint, a gyro and an odometer are weighted together using an EKF (Extended Kalman Filter) to estimate the position. Laser scans from two laser scanners are then compared with the map using UKF (Unscented Kalman Filter) to update the position estimate. Deviation from the desired route point is used as input to a control algorithm that steers the LHD towards the route point in the desired speed. The system is built to operate in an obstacle free environment, but simple obstacle avoidance algorithms are built in the system to make the machine stop if obstacles come in its way.

1.3 Objective

All of the sensors need calibration because of errors from high tolerances in the machine construction. This project focuses on calibration of the hinge angle sensor and the laser scanners. The hinge angle sensor is used to measure the angle between the front and rear part. A method was searched that could find an angle offset that when applied reduces it to within $\pm 0.2^{o}$. Before this project it was required that someone climbed on the back of the LHD and tried to align the machines back- and front end while the LHD was moving. When aligned one was able to get a reading of the angular offset.

To get correct maps it's important that the orientation of laser scanners relative the LHD:s coordinate system is known. This project is focused on the laser heading, which is the most critical parameter. The goal was to find the angular offsets of the laser scanners to give a maximum scan matching error less than a predefined value of 0.35. Before this project the lasers heading where manually put to zero by eye sighting.

1.4 Contribution

A new method is here proposed that can be used on any centre articulated vehicle to automatically find the offset of the hinge angle sensor. It uses the kinematic model in (Ridely & Corke 2001) together with the hinge angle sensor, the gyro and the odometer to get an estimate of the hinge angle offset. Error propagation was made to get an early estimate of the accuracy of the method. Different confidence intervals were then estimated to be able to guarantee its performance. Experiments have shown that the method delivers a hinge angle offset with an accuracy of $\pm 0.3^{o}$. The requirement is that the machine is driven straight at least 33 m at 2.5 m/s

A new method is here proposed that can be used to find the angular offset of a number of lasers on a moving vehicle automatically. It uses an augmentation of the original vehicle model, an EKF for prediction, an UKF for filtering and a SLAM (Simultanoues Localization and Mapping) algorithm. No error propagation nor a confidence interval were calculated for the laser offset because the method was too complex and too few data existed to get a good enough confidence interval. Experiments have verified that if the vehicle is driven straight in a 23 m normal sized mine drift it can estimate the angular offsets of two lasers to within $\pm 0.5^{o}$, which is need to get a maximum scan matching error less than a predefined value of 0.35.

1.5 Report structure

In Chapter 2 the report evaluates different ideas before going through the sensors, algorithms and methods used for finding the offsets of both the lasers and the hinge angle sensor in Chapter 3. After going through the methods it continues with dealing with how the driving and sensor measurements affect the accuracy of the estimated hinge angle in Chapter 4. It then goes through the real experiments done to verify the accuracy of the system and its results in Chapter 5. The report then proceeds with taking up the required angular

accuracy of the laser offset estimation deduced from the given laser scan matching error in Chapter 6. In Chapter 7 it investigates the true accuracy found from test made in real environments and ends with a conclusion and future work in Chapter 8.

2 Requirements and approach

A literature research was made to find previous work in the area. For both problems, which were estimating the hinge angle offset and the laser scanner offsets, ideas were put-up and evaluated to find the best working methods that for filled the following requirements:

- Deliver estimates with high enough accuracy.
- Not need any surrounding equipment or extra sensors.
- Be easily handled by the machine operator.
- Operate in mine drifts that are 50 m or shorter, because mine drifts are often short.
- Need a time less than 30 minutes for calculations.

2.1 Hinge angle offset

The hinge angle sensor has before this project been calibrated using the method described in Chapter 1.3. It delivered an offset in the range of $\pm 0.2^{o}$, which has shown to be good enough for the system to operate without problems, because of that we require that the new hinge angle calibration method should deliver an offset in the same range. Different cases similar to this were investigated. Martinelli et. al. (2003), Madhavan, Dissanayake & Durrant-Whytel (1998) and Dall Larsen, Bak, A. Andersen & Ravn (1998) used EKF and AKF (Augmented Kalman filter) for online training to estimate constant errors. The first two used an onboard laser scanner and the last one camera measurements fused together with odometry measurements as inputs. Borenstein (1996) and De Ceccco (2002) used special drive patterns together with absolute measurements from surrounding equipment to calculate the odometric parameters.

Tests were made to only use the hinge angle for calibration but it became unpractical. Instead it was decided to use the gyro and the odometer. Their data is quite easy to analyse compared to the laser data and it contains all the information needed for calibrating the hinge angle sensor. The odometer and gyro can also easily be calibrated before the hinge angle sensor. Calibrating a hinge angle sensor on similar vehicles with help of a gyro and an odometer has never been done before so some new ideas were born. The final idea was to use a kinematic model of a centre articulated vehicle to calculate the hinge angle offset from the rotation speed given by the gyro and the transitional speed estimated from the odometer. Due to the simple calculations the computation time is less than a minute. More about the ideas can be read in Appendix A.

2.2 Laser offsets

A literature research showed that there didn't exist any earlier work in the area of estimating the laser scanners angular offset. The closest work were the constant model error estimation in (Martinelli, Tomatis, Tapus, & Siegwart 2003) and (Madhavan, Dissanayake & Durrant-Whytel 1998) which uses EKF on laser data together with augmentation of the states.

When estimating the laser offsets the laser measurements needs to be used, which increases the level of complexity compared to the hinge angle calibration case. One alternative was to by brute force test all positive combinations of laser offsets to see which two gave the smallest scan matching error but early experiments showed that it took too long time. The system is built around an EKF together with an UKF so a natural choice was to use them together with state augmentation to estimate the laser offset parameters.

A problem with this solution was that the map needs to be known a priori, which isn't always the case. To solve this problem we needed to implement SLAM. UKF based SLAM can be seen in (Martinez-Cantin & Castellanos 2005), which is one of many that uses one state for each feature. The original system uses a grid map and thereby the feature space become to large if each grid point should be represented by one state variable. A solution to this was created in (Merwe, Doucet, Freitas & Wan 2000) using a more complex particle filter. Instead of using it, it was concluded that one could create a less complex algorithm that reused the existing mapping algorithm together with the EKF and UKF. The computations of this method are still heavy and depend on a number of parameters but its faster than brute force search.

3 Theory and methods

This chapter goes through the theory and methods used for estimating the hinge angle offset and the laser scanners angular offset. The chapter begins with going through the kinematic model of the centre articulated LHD in chapter 3.1 and then continues with the sensors used in Chapter 3.2. Chapter 3.3 goes through the hinge angle offset estimation and its error analysis together with the statistics used for calculation of the confidence intervals. Chapter 3.4 then continues with estimation of the laser scanners offset using EKF and UKF in a SLAM algorithm. The chapter ends with a brief walk-through of the implementation of the two methods and also the simulator used for creating simulated log-files.

3.1 Kinematic model

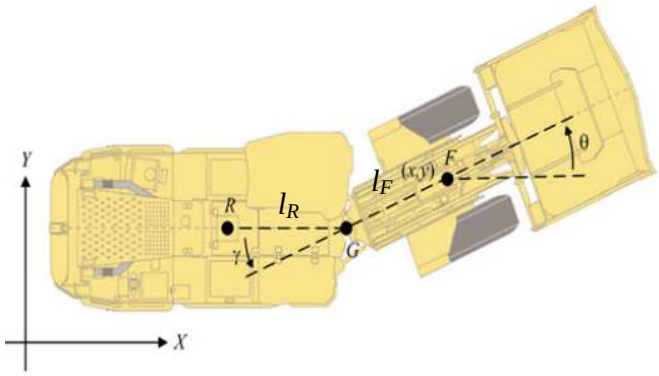

Figure 1: Model of a centre-articulated vehicle.

The kinematic model of the LHD already in use in the system assumes no slip and can be found in a number of papers (Altafini 1999) and (Ridely & Corke 2001). It uses the setup seen in Figure 1 where γ is the angle between the centre lines of the two bodies. θ, θ_R is the heading of the front and rear body respectively in relation to the x-axis of the global coordinate system. l_F is the distance between the hinge *G* and the front axle centre *F* and l_R the distance between the hinge *G* and the rear axle centre *R*. The models for the rotation of the LHD are

$$\dot{\theta} = \frac{v \sin\gamma + l_R \dot{\gamma}}{l_F \cos\gamma + l_R} \qquad (1)$$

and

$$\dot{\theta}_R = \frac{v \sin\gamma - l_F \dot{\gamma} \cos\gamma}{l_F \cos\gamma + l_R} \qquad (2)$$

where *v* is the speed of the front body. From the model it can be concluded that the rotation increases in magnitude with speed, hinge angle and if the hinge is rotated $\dot{\gamma} \neq 0$. The rotation also decreases with increased machine length.

The LHD has four wheel drive. There are separate differentials for the front and rear wheels but a stiff driveshaft connects between the two differentials. This makes the front and back wheels get the same speed. According to the model they shouldn't have the same speed if $l_F \neq l_R$ or the vehicle is not driving straight, $\gamma \neq 0$, and thereby is a slippage introduced when γ is increased. So the models performance decreases with increased γ.

In Ridely & Corke (2001) one error was found in Eq. (2) where they had missed the multiplication with $\cos\gamma$, which was proven by simple calculations and later confirmed by reading Altafini (1999).

The nonlinear discrete time state space model in Marshall, Barfoot, & Larsson (2008) is created from a continuous one using Euler steps giving

$$\mathbf{s}(n+1) = \mathbf{\Phi}_s \mathbf{s}(n) + \mathbf{\Gamma}_u(\mathbf{s}(n)) \cdot (\mathbf{u}(n) + \mathbf{v}(n)), \quad (3)$$

$$\mathbf{s}(n) = \begin{bmatrix} x(n) \\ y(n) \\ \theta(n) \\ \gamma(n) \end{bmatrix}, \ \mathbf{u}(n) = \begin{bmatrix} v(n) \\ \omega(n) \end{bmatrix}$$

where

$$\mathbf{\Gamma}_u(\mathbf{s}(n)) = \begin{bmatrix} h\cos\theta(n) & 0 \\ h\sin\theta(n) & 0 \\ \dfrac{-h\sin\gamma(n)}{l_F\cos\gamma(n)+l_R} & \dfrac{-hl_R}{l_F\cos\gamma(n)+l_R} \\ 0 & h \end{bmatrix}$$

$\mathbf{v}(n)$ is model errors and other uncertainties and assumed to be Gaussian noise

$$\mathbf{v}(n) \sim N(\mathbf{0}, \mathbf{Q})$$

with covariance

$$\mathbf{Q} = \begin{bmatrix} \sigma_v^2 & 0 \\ 0 & \sigma_\omega^2 \end{bmatrix}$$

h in the model is equal to the sampling time and $\omega(n)$ is equal to the angular speed of the hinge angle $\dot{\gamma}(n)$. The state update matrix $\mathbf{\Phi}_s$ is the identity matrix because we don't model the dynamics.

3.2 Sensors

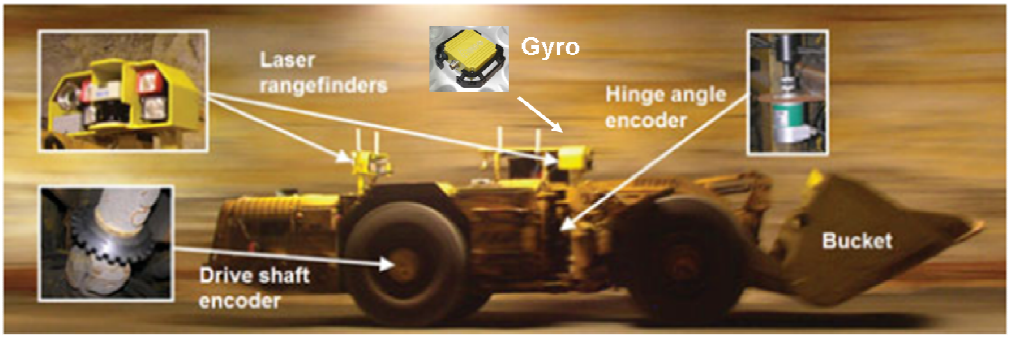

Figure 2: The LHD and its sensors.

As seen in Figure 2 the LHD is equipped with a hinge angle sensor to measure the angle between the front and rear part. It uses and odometer mounted on the driveshaft in order to measure the speed and the distance travelled. Mounted on the top of the machine are two laser scanners used to map the surrounding and position the LHD. One of the scanners is mounted backwards on the rear part

and one is mounted forward on the front part. Together with the front laser an IMU (Inertial Measurement Unit) is mounted, containing a heading gyro to measure the rotation of the front part.

3.2.1 IMU Navigation02

The IMU Navigation02 is delivered by the company AIMS. It has three gyros with 24 bits resolution each giving angular speed resolution of $16\mu^o/s$. The following parameters can be found for the gyros:

- Range ±120 °/s
- Bias Error 0.06 °/s (1 σ)
- Scale Factor Error 0.25 % (1 σ)
- Non-linearity 0.5 % of FS
- Noise 0.1 °/s (Broadband RMS)
- Bandwidth 25 Hz
- Misalignment 5 mrad

It's only the heading gyro that is used and a simple model of its measurements is

$$\dot{\theta}_m(n) = \dot{\theta}(n) + \dot{\theta}_b + v_{\dot{\theta}_m}(n)$$

where

$$v_{\dot{\theta}_m}(n) \sim N(0, \sigma^2_{\dot{\theta}_m}(n))$$

and

$$\sigma_{\dot{\theta}_m}(n) = 120 * 0.005/3 + 0.0025\dot{\theta}(n) + 0.001 = 0.3\% + 0.0025\dot{\theta}(n).$$

$\dot{\theta}(n)$ is the true angular speed, $\dot{\theta}_b$ is the bias error and $v_{\dot{\theta}_m}(n)$ is the Gaussian noise affecting the measurements. The non-linearity and the scale factor are modelled as Gaussian noise even though they are constant for each unique IMU unit. Reasons for modelling them as Gaussian noise are that they aren't known and that they vary with the size of $\dot{\theta}_b$ so Gaussian noise is the closest approximation. It's approximated that three standard deviations contains all errors and that is why the non-linearity is divided by three to get one standard deviation. The bias $\dot{\theta}_b$ is instead modelled as a constant because of that it's later estimated and removed in the analysis and its sample variance is small. Misalignment is approximated to be zero due to its small size. It should also be mentioned that the IMU is mounted in a rubber suspension to remove some vibrations.

3.2.2 Odometer

The odometer is base on a driveshaft encoder that measures the number of teeth passing by to calculate the distance travelled. It uses the fact that if the distance between the teeth, the radius of the wheels and the number of teeth passed are known the distance travelled d_m can be determined. The mounting on the driveshaft makes the odometer insensible to turns.

The odometer system consists of three parts, an encoder, an I/O module and the machine computer, which is illustrated in Figure 3. The I/O module checks the encoder pulse counter every 5 ms and the machine computer then checks the I/O module around every system sampling time *h*, equal with 40 ms. This makes it possible that the value in the I/O module is up to 5 ms old. When calculating the distance travelled the system calculate it as 40 ms has gone between two samples, which then isn't always true. The error can never grow larger than a time error of around 5 ms.

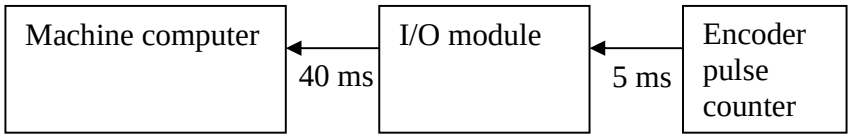

Figure 3: Odometer sample flow from sensor to machine computer

The measured speed v_m is estimated from d_m using the model

$$v_m(n) = \frac{d_m(n) - d_m(n-1)}{h} = \frac{v(n)h \pm v(n) * 5 * 10^{-3}}{h} = v(n) \pm \frac{v(n) * 5 * 10^{-3}}{h}.$$

It's approximated that the synchronization error in each sample is zero mean Gaussian. According to the Gaussian distribution $3\sigma_{v_m} \approx$ max error which makes

$$\sigma_{v_m}(n) = \frac{v(n) * 5 * 10^{-3}}{3h}.$$

Drift due to slip is approximated to be zero according to previous measurements done with the machine. Also the radius of the wheels is said to be known without errors.

3.2.3 Hinge angle sensor

The hinge angle sensor is an encoder mounted in the joint holding the front and rear body together. The encoders range is $(0,360]^o$ and it has 16 bits resolution giving an angular resolution of 6 millidegrees. Previous measures have shown that the angular measurements $\gamma_m(n)$ have a Gaussian noise $v_{\gamma_m}(n)$, which have a standard deviation σ_{γ_m} of approximately 0.01^o. The hinge angle sensor is mounted to give approximately 180^o when the machine is straight. 0^o is wanted so the offset γ_o is 180^o under ideal conditions but there is also a mounting error that introduces an offset. The machine can operate in the range

[-45,45]^o where 0^o is when the machine is straight. A measurement from the hinge angle can be modelled as

$$\gamma_m(n) = \gamma(n) + \gamma_o + v_{\gamma_m}(n) \quad (4)$$

where $\gamma(n)$ is the true hinge angle and

$v_{\gamma_m}(n) \sim N(0, \sigma^2_{\gamma_m})$.

3.2.4 SICK Laser scanner

The SICK laser uses a moving laser beam to scan the environment in one plane. It has a maximum scanning range of 32 m in the interval [-90, 90]^o degrees with an angular resolution of 1^o giving N_{points}=181 scans. A laser beam i where i=1,…, N_{points} can be modelled as

$$z_m(i) = z_{spot}(i) + z_{ci} + v_z(i)$$

where

$v_z(i) \sim N(0, \sigma^2_z)$.

z_{ci} is a constant error in the range [0,0.03] m and σ_z =0.01 m is the stochastic error. The laser beam creates a spot, with aperture angle 0.11 milliradians, that increases with distance and angle to the objects normal. $z_{spot}(i)$ is the distance to the closest point on the object hit by the laser beam.

3.3 Hinge angle offset

3.3.1 Estimation of the hinge angle offset γ_o

The idea is to rearrange Eq. (1) in Chapter 3.1 to get an expression for the hinge angle and then use it for estimation of the hinge angle offset γ_o.

Estimation is made by using the unbiased rotation speed $\hat{\dot{\theta}}_{ubm}(n)$ measured by the heading gyro, the measured speed $v_m(n)$ and the hinge angle measurement $\gamma_m(n)$, where n=1,…,N is the number of measurements. To simplify the rearrangement estimation is done only for the rotation created from forward motion and not from change in hinge angle. $\dot{\gamma}$ is therefore put to zero and Eq. (1) is rearranged to give

$$v \sin\gamma - \dot{\theta} \cdot l_F \cos\gamma = \dot{\theta} \cdot l_R .$$

It is known that adding two sinusoidal waves with the same frequency and different phase gives a new wave with the same frequency but a new phase and amplitude. For example

$$a \sin x + b \cos x = \sqrt{a^2 + b^2} \sin(x + \varphi)$$

where

$$\varphi = \tan^{-1}\left(\frac{b}{a}\right) + \begin{cases} 0 & if \quad a \geq 0 \\ \pi & if \quad a < 0 \end{cases}$$

Applying this makes it possible to get only one γ in the equation

$$\sqrt{v^2 + \left(\dot{\theta}_F l_R\right)^2}\,\sin\left(\tan^{-1}\left(\frac{-\dot{\theta} l_F}{v}\right) + \gamma\right) = \dot{\theta} l_R \,.$$

Solving for γ gives

$$\gamma = \sin^{-1}\left(\frac{\dot{\theta} l_R}{\sqrt{v^2 + \left(\dot{\theta} l_R\right)^2}}\right) + \tan^{-1}\left(\frac{\dot{\theta} l_F}{v}\right) \qquad (5)$$

and for negative *v*

$$\gamma = -\sin^{-1}\left(\frac{\dot{\theta} l_R}{\sqrt{v^2 + \left(\dot{\theta} l_R\right)^2}}\right) + \tan^{-1}\left(\frac{\dot{\theta} l_F}{v}\right). \qquad (6)$$

The rotation $\hat{\dot{\theta}}_{ubm}(n)$ includes both the rotation caused by the speed $v(n)$ and by $\dot{\gamma}(n)$. To remove the rotation caused by $\dot{\gamma}(n)$ we use the approximation

$$\hat{\dot{\gamma}}(n) \approx \frac{\gamma_m(n) - \gamma_m(n-1)}{h}$$

which is independent of γ_o and thereby only contains the articulation rate plus some noise. The approximation is used in the non-speed part (*v* equal zero) of Eq. (1) and is then subtracted from $\hat{\dot{\theta}}_{ubm}(n)$ giving

$$\dot{\theta}_v(n) = \hat{\dot{\theta}}_{ubm}(n) - \frac{l_R \hat{\dot{\gamma}}(n)}{l_F \cos\hat{\gamma}(n) + l_R}\,. \qquad (7)$$

where $\hat{\gamma}(n)$ is an estimate of the true hinge angle.

If $\gamma_m(n)$ is used as $\hat{\gamma}(n)$ it introduces an error in the final offset estimate $\hat{\gamma}_o$ because of the offset. The error introduced is limited as long as γ_o is reasonably close to zero but that isn't always the case because the offset γ_o can be between (-180, 180]°. From the analysis in Chapter 4.2 it has been found that if the whole algorithm is iterated m=1,…,M times and $\hat{\gamma}(n)$ is estimated from $\gamma_m(n)$ by removing the previous offset estimate $\hat{\gamma}_o(m\text{-}1)$ the offset estimate $\hat{\gamma}_o(m)$ converges towards the true offset γ_o. Given that the vehicle is driven along a straight line a first estimate of $\hat{\gamma}_o$ can be calculated from

$$\hat{\gamma}_o(0) = \frac{1}{N}\sum_{i=1}^{N}\gamma_m(i).$$

The difference between $\hat{\gamma}_o(0)$ and the true offset γ_o is then the mean of the true hinge angle $\gamma(n)$ as seen by taking the mean of Eq. (4)

$$\hat{\gamma}_o(0) = mean(\gamma_m(n)) = mean(\gamma(n)) + mean(\gamma_o) + mean(v_\gamma(n)) \quad (8)$$
$$= mean(\gamma(n)) + \gamma_o$$

If the vehicle is driven straight the mean of $\gamma(n)$ is zero and the approximation is exact. In reality this is impossible, which implies that an error still remains. The above discussion gives the following conclusion

$$\hat{\gamma}(n) = \begin{cases} \gamma_m(n) - mean(\gamma_m(n)) & if \quad m = 0 \\ \gamma_m(n) - \hat{\gamma}_o(m-1) & if \quad m > 0 \end{cases}$$

By inserting $\dot{\theta}_v(n)$ and $v_m(n)$ into Eq. (5) or Eq. (6) the hinge angle, now called $\gamma_{\dot{\theta},v}(n)$, is found. The estimated sample offset $\hat{\gamma}_{so}(n)$ is then given by

$$\hat{\gamma}_{so}(n) = \gamma_m(n) - \gamma_{\dot{\theta},v}(n) \quad (9)$$

and includes noise from $\dot{\theta}_v(n)$, $v_m(n)$ and $\gamma_m(n)$. By taking the mean of all $\hat{\gamma}_{so}(n)$ from the whole data set

$$\hat{\gamma}_o(m) = \frac{1}{N}\sum_{i=1}^{N}\hat{\gamma}_{so}(i) \quad (10)$$

the best estimate of the hinge angle offset $\hat{\gamma}_o(m)$ is found. This should then be repeated M times.

3.3.2 Estimation of gyro bias

The rotation speed $\dot{\theta}_m(n)$ measured by the gyro includes a bias $\dot{\theta}_b$ that is temperature dependent and thereby changes over time due to temperature changes in the IMU. The change over a short time period, as a calibration run, is small and the bias can be estimated when the machine stands still as the mean of $\dot{\theta}_m(i)$ giving

$$\hat{\dot{\theta}}_b = \frac{1}{N_0}\sum_{N_0}\dot{\theta}_m(i) \qquad i=1,\ldots,N_0$$

where N_0 is the number of measurements when standing still. The measurements is then compensated to form unbiased measurement estimates

$$\hat{\dot{\theta}}_{ubm}(n) = \dot{\theta}_m(n) - \hat{\dot{\theta}}_b$$

that can be used for the calibration.

3.3.3 Error propagation

Using error propagation the propagation of the stochastic errors through the hinge angle method can be analysed. By inserting combinations of $\hat{\dot{\theta}}_{ubm}(n)$, $v_m(n)$, $\gamma_m(n)$ and the number of measurements N the variance of $\hat{\gamma}_o$ can be found. It should be remembered that this requires that the model is correct and thereby doesn't the analysis give any information regarding effects from errors in the model.

In Eq. (7) the measurement error in all parameters are independent. The error propagation through Eq. (7) can then be estimated using

$$\sigma_{\dot{\theta}_v}^2 = \left|\frac{\partial \dot{\theta}_v}{\partial \hat{\dot{\theta}}_{ubm}}\right| \sigma_{\dot{\theta}_m}^2 + \left|\frac{\partial \dot{\theta}_v}{\partial \gamma_m}\right| \sigma_{\gamma_m}^2 + \left|\frac{\partial \dot{\theta}_v}{\partial \gamma_{m-1}}\right| \sigma_{\gamma_m}^2$$

where

$$\frac{\partial \dot{\theta}_v}{\partial \hat{\dot{\theta}}_{ubm}} = 1,$$

$$\frac{\partial \dot{\theta}_v}{\partial \gamma_m} = -l_2 h \frac{l_2 + l_1 \cos\gamma_m + l_1(\gamma_m - \gamma_{m-1})\sin\gamma_m}{(l_2 + l_1\cos\gamma_m)^2}$$

and

$$\frac{\partial \dot{\theta}_v}{\partial \gamma_{m-1}} = \frac{l_2}{h(l_2 + l_1\cos\gamma_m)}.$$

In Eq. (5) the measurement errors are also independent giving

$$\sigma_{\gamma_{\dot{\theta},v}}^2 = \left|\frac{\partial \gamma_{\dot{\theta},v}}{\partial \dot{\theta}_v}\right| \sigma_{\dot{\theta}_v}^2 + \left|\frac{\partial \gamma_{\dot{\theta},v}}{\partial v_m}\right| \sigma_{v_m}^2$$

where

$$\frac{\partial \gamma_{\dot{\theta},v}}{\partial \dot{\theta}_v} = \frac{1}{\sqrt{1 - \frac{\dot{\theta}_v^2 l_2^2}{v^2 + \dot{\theta}_v^2 l_1^2}}} \frac{l_2\sqrt{v^2 + \dot{\theta}_v^2 l_1^2} - \left(v^2 + \dot{\theta}_v^2 l_1^2\right)^{-\frac{1}{2}} l_1^2 l_2 \dot{\theta}_v^2}{v^2 + \dot{\theta}_v^2 l_1^2} + \frac{l_1}{v + \frac{\dot{\theta}_v^2 l_1^2}{v}}$$

and

$$\frac{\partial \gamma_{\dot{\theta},v}}{\partial v_m} = \frac{-1}{\sqrt{1 - \frac{\dot{\theta}_v^2 l_2^2}{v^2 + \dot{\theta}_v^2 l_1^2}}} \frac{\dot{\theta}_v l_2 v}{\left(v^2 + \dot{\theta}_v^2 l_1^2\right)^{\frac{3}{2}}} - \frac{l_1 \dot{\theta}_v}{v^2 + \dot{\theta}_v^2 l_1^2}.$$

The above equations holds for each measurement n=1,…,N. The total variance of the estimated offset $\hat{\gamma}_o$ is then from Eq. (10)

$$\hat{\sigma}^2_{\hat{\gamma}_o} = \frac{1}{N^2}\sum_{n=1}^{N}\left(\left(\sigma^2_{\gamma_{\dot{\theta},v}}(n)+\sigma^2_{\gamma_m}(n)\right)+2\rho_{\gamma_{\dot{\theta},v},\gamma_m}(n)\sigma^2_{\gamma_{\dot{\theta},v}}(n)\sigma^2_{\gamma_m}(n)\right). \quad (11)$$

γ_m is in Eq. (7) and in Eq. (9) which implies that there is a correlation $\rho_{\gamma_{\dot{\theta},v},\gamma_m}$. The variance $\sigma^2_{\hat{\gamma}_o}$ is largest when $\rho_{\gamma_{\dot{\theta},v},\gamma_m}=1$ but experiments have shown that the effect of the correlation is small.

Using $\hat{\sigma}_{\hat{\gamma}_o}$ one could estimate a 99 % confidence interval for the $\hat{\gamma}_o$. The sensors have Gaussian errors and therefore the error on $\hat{\gamma}_o$ is also Gaussian. Using the Gaussian distribution the confidence interval is given by

$$\hat{\gamma}_o - 2.576\hat{\sigma}_{\hat{\gamma}_o} < \gamma_o < \hat{\gamma}_o + 2.576\hat{\sigma}_{\hat{\gamma}_o}$$

3.3.4 Measurement statistics

By repeating the same experiment N_1 times and each time collect N_2 measurements the 99 % confidence interval of the hinge angle method can be found. There exist two methods to calculate the confidence interval.

The first method begins with calculating the estimated standard deviation $s_{\hat{\gamma}_{so}}(p)$, where p=1,…,N_1, of the sample offsets $\hat{\gamma}_{so}(n)$ using

$$s_{\hat{\gamma}_{so}}(p) = \sqrt{\frac{1}{N_2-1}\sum_{n=1}^{N_2}\left(\hat{\gamma}_o(p)-\hat{\gamma}_{so}(n)\right)^2}$$

where n=1,…,N_2 is the number of samples in each experiment. If N_2 is large an approximation can be made that $s_{\hat{\gamma}_{so}}(p)$ is equal to the true standard deviation $\sigma_{\hat{\gamma}_{so}}(p)$ of the whole population and thereby having a Gaussian distributed and not a Student-t distribution.

We assume that the spread of $\hat{\gamma}_o(p)$ is not correlated as a result of that the measurement noise can be assumed to be white Gaussian noise. Then the estimated standard deviation of the $\hat{\gamma}_o(p)$ from all N_2 measurements is given by

$$\sigma_{\hat{\gamma}_{o1}}(p) = \frac{1}{\sqrt{N_1}}\sigma_{\hat{\gamma}_{so}}(p). \quad (12)$$

According to the Gaussian distribution one could know with 99 % confidence that the true offset γ_o is in the interval

$$\hat{\gamma}_o - 2.576\sigma_{\hat{\gamma}_{o1}}(p) < \gamma_o < \hat{\gamma}_o + 2.576\sigma_{\hat{\gamma}_{o1}}(p).$$

This should be tested for all N_1 experiments. One experiment had been enough in the ideal world to assure the statistics but more experiments with the same

setup are made to confirm the result. The interval should be smaller than $\pm 0.2^{o}$ to confirm that the method is good enough. Ideally it should be enough to increase N_2 to get into that interval. Also if the spread is correlated $\sigma_{\hat{\gamma}_o 1}(p)$ is going to be smaller than the true standard deviation.

The second method calculates the standard deviation of $\hat{\gamma}_o(p)$ directly. To begin with the mean of all $\hat{\gamma}_o(p)$ is

$$\bar{\hat{\gamma}}_o = \frac{1}{N_1}\sum_{p=1}^{N_1}\hat{\gamma}_o(p)$$

and the estimated standard deviation is then

$$s_{\hat{\gamma}_o} = \sqrt{\frac{1}{N_1 - 1}\sum_{p=1}^{N_1}\left(\hat{\gamma}_o(p) - \bar{\hat{\gamma}}_o\right)^2}\ .$$

Due to that N_1 is relatively small $s_{\hat{\gamma}_o}$ has an uncertainty. If the spread is Gaussian, $s_{\hat{\gamma}_o}$ has a χ^2 distribution and the 99 % confidence interval of $s_{\hat{\gamma}_o}$ is

$$L_1 = \sqrt{\frac{(N_1 - 1)s_{\hat{\gamma}_o}^2}{\chi^2_{0.99/2,N_1-1}}} < \sigma_{\hat{\gamma}_o 2} < L_2 = \sqrt{\frac{(N_1 - 1)s_{\hat{\gamma}_o}^2}{\chi^2_{1-0.99/2,N_1-1}}}\ .$$

The confidence interval of γ_o is then

$$\bar{\hat{\gamma}}_o - 2.576L_2 < \gamma_o < \bar{\hat{\gamma}}_o + 2.576L_2$$

This method only relies on that the spread is Gaussian and is therefore more reliable. It gives a larger confidence interval due to the uncertainty in $\sigma_{\hat{\gamma}_o 2}$. The uncertainty can be decreased by increasing N_1. When N_1 goes to infinity the confidence interval decreases to the true confidence interval.

One could compare $s_{\hat{\gamma}_o}$ with each of the N_1 estimated standard deviations $\sigma_{\hat{\gamma}_o 1}$ by assuming that $s_{\hat{\gamma}_o}$ is the true standard deviation and using the fact that $s_{\hat{\gamma}_o}$ is the spread of the $\hat{\gamma}_o(p)$:s around $\bar{\hat{\gamma}}_o$. This gives

$$\frac{\chi^2}{N_1 - 1} = \frac{1}{N_1 - 1}\sum_{p=1}^{N_1}\frac{1}{\sigma^2_{\hat{\gamma}_o 1}}(\hat{\gamma}_o(p) - \bar{\hat{\gamma}}_o)^2\ . \qquad (13)$$

If $\frac{\chi^2}{N_1 - 1} > 1$ than $\sigma_{\hat{\gamma}_o 1} < s_{\hat{\gamma}_o}$ and we have under estimated the standard deviation using the first method. This means that the spread is probably not uncorrelated. $\frac{\chi^2}{N_1 - 1}$ can be use to scale $\sigma_{\hat{\gamma}_o 1}$ to its true value but it should be remembered that Eq. (13) doesn't take in to consideration that $s_{\hat{\gamma}_o}$ is an uncertain estimate of $\sigma_{\hat{\gamma}_o}$ if N_1 is small.

3.4 Laser scanners angular offset

3.4.1 Creating and evaluating the map

Under normal operation is the map **M** created under Route Profiling from the log data, containing all the sensor data recorded under the teaching step. To create **M** the log is gone through step by step to estimated ***u(n)*** using backward Euler on γ_m and d_m. ***u(n)*** is then input to Eq. (3) to get the pose ***s(n)*** of the machine at each time step. The map, which is represented by a 2 dimensional binary grid is then finally updated using ray tracing along the recorded laser beams at each position ***s(n)*** for both the front and rear laser.

After creation a simulated Playback is made in the map to evaluate it using the logged data as input. In the simulation the logged laser beams' lengths are compared to the simulated ones. From the comparison over all samples a scan matching error ε_{match} is calculated. If the map is identical to the real world the machine should get identical laser scans and ε_{match} equal to zero. The ε_{match} must at all times be under 0.35 for the map to be acknowledged.

3.4.2 State estimation using nonlinear Kalman filter

To keep track of the machine under playback the state $\mathbf{s}(n)$ needs to be estimated at each sample time. A good prediction of the state can be found by using the kinematic state space model in Eq. (3). To get better accuracy and compensate for drift the state is then filtered with help of the measured laser data. This method of first predicting using a model and then update using measured data is called Kalman Filtering. A standard Kalman Filter can only operate on linear equations. For nonlinear equations there exist a number of different solutions. This machine uses a mix of two Kalman Filters, an EKF (Extended Kalman Filter) for prediction and an UKF (Unscented Kalman Filter) for filtering. The implementation of the EKF and UKF used can be seen in (Marshall, Barfoot, & Larsson 2008). To simplify notation let $\hat{\mathbf{s}}^{-}(n)$ be the prediction of the state using EKF and $\hat{\mathbf{s}}(n)$ the filtered estimate of the state using UKF. In the same way let $\mathbf{P}^{-}(n)$ be the predicted state covariance and $\mathbf{P}(n)$ be the filtered covariance.

To solve the problem that the Kalman filter needs linear equations the Extended Kalman Filter uses linearization of the state equation Eq. (3) around the previous state. Eq. (3) is linearized to get

$$\hat{\mathbf{s}}^{-}(n) = \mathbf{H}_s(\hat{\mathbf{s}}(n-1)) \cdot \hat{\mathbf{s}}(n-1) + \mathbf{\Gamma}_u(\hat{\mathbf{s}}(n-1)) \cdot \mathbf{u}(n). \qquad (14)$$

where

$$\mathbf{H}_s(\mathbf{s}(n-1)) = \left.\frac{\partial \mathbf{\Phi}_s}{\partial \mathbf{s}}\right|_{\bar{\mathbf{s}}_{n-1},\mathbf{u}_n} =$$

$$= \begin{bmatrix} 1 & 0 & -hv(n)\sin(\theta(n-1)) & 0 \\ 0 & 1 & hv(n)\cos(\theta(n-1)) & 0 \\ 0 & 0 & 1 & \dfrac{-hl_R v(n)\cos(\gamma(n-1)) - v(n)l_F}{(l_R + l_F\cos(\gamma(n-1)))^2} - \dfrac{h\omega(n)l_R l_F \sin(\gamma(n-1))}{(l_R + l_F\cos(\gamma(n-1)))^2} \\ 0 & 0 & 0 & 1 \end{bmatrix}$$

The covariance of the estimate is calculated as

$$\mathbf{P}^-(n) = \mathbf{\Gamma}_u(\hat{\mathbf{s}}(n-1)) \cdot \mathbf{Q} \cdot \mathbf{\Gamma}_u^T(\hat{\mathbf{s}}(n-1)) + \mathbf{H}_s(\hat{\mathbf{s}}(n-1)) \cdot \mathbf{P}(n-1) \cdot \mathbf{H}_s^T(\hat{\mathbf{s}}(n-1)). \quad (15)$$

$\mathbf{s}(0)$ is set to a by the user predicted state and $\mathbf{P}(0)$ is set to the initial covariance of that state. $\mathbf{Q}$ is the covariance in the inputs defined in Chapter 3.1.

To use an EKF for the filter step the state-to-output matrix ***G*** is needed, which maps the states to the laser measurements. ***G*** is to complex to express explicit and because of that Unscented Kalman Filtering is used instead. Numerical methods could have been used to estimate ***G*** but in (Simon 2006) it's shown that UKF gives higher order estimation than EKF, which only gives a first order. UKF also simplifies the estimation. As stated in (Simon 2006) UKF is based on the two facts. The first is that it is easy to perform a nonlinear transformation on single points. The second fact is that it is not too hard to find a set of individual points in a state space whose sample probability density function approximate the true probability density function of the states.

The UKF uses 2*N*+1 points, called sigma-points, which is found using the covariance $\mathbf{P}^-(n)$ and put into a matrix

$$\tilde{\mathbf{S}}(n) = \left[\hat{\mathbf{s}}^-(n) \quad \hat{\mathbf{s}}^-(n) + \chi\sqrt{\mathbf{P}^-(n)} \quad \hat{\mathbf{s}}^-(n) - \chi\sqrt{\mathbf{P}^-(n)}\right]. \quad (16)$$

N is the number of state variables and

$$\chi = \sqrt{N + \lambda}$$

where

$$\lambda = \alpha^2(N + \kappa) - N.$$

κ is a constant often chosen to 0 and α is constant in the range [0.001,1].

At each sigma-point, represented by the columns in $\tilde{\mathbf{S}}(n)$, an artificial laser scan is made in the map $\mathbf{M}$ to form a matrix $\tilde{\mathbf{Z}}(n)$. From $\tilde{\mathbf{Z}}(n)$ the mean is calculated for each beam direction over all laser scans as

$$\bar{\mathbf{z}}(n) = \sum_{i=0}^{2N} w_{m,i} \tilde{\mathbf{Z}}_i(n) \quad (17)$$

where

$$w_{m,i} = \begin{cases} \lambda/(N+\lambda) & i = 0 \\ 1/(2(N+\lambda)) & i \neq 0 \end{cases}.$$

Using the mean, the covariance of the artificial measurements is calculated as

$$\mathbf{Z}(n) = \sum_{i=0}^{2N} w_{c,i} \left(\tilde{\mathbf{Z}}_i(n) - \bar{\mathbf{z}}(n)\right)\left(\tilde{\mathbf{Z}}_i(n) - \bar{\mathbf{z}}(n)\right)^T + \mathbf{R} \quad (18)$$

where

$$w_{c,i} = \begin{cases} \lambda/(N+\lambda) + (1-\alpha^2+\beta) & i = 0 \\ 1/(2(N+\lambda)) & i \neq 0 \end{cases}.$$

β is typically 0 and $\mathbf{R} = \delta^2 \mathbf{I}$ is a diagonal matrix with each diagonal element equal to the variance of each scan line. To get a relation between the state change and the change in the artificial laser measurements the covariance between them is calculated as

$$\mathbf{J}(n) = \sum_{i=0}^{2N} w_{c,i} \left(\tilde{\mathbf{Z}}_i(n) - \bar{\mathbf{z}}(n)\right)\left(\tilde{\mathbf{S}}_i(n) - \bar{\mathbf{s}}(n)\right)^T. \quad (19)$$

Using $\mathbf{Z}(n)$ and $\mathbf{J}(n)$ the update matrix is calculated as

$$\mathbf{K}(n) = \mathbf{J}^T(n)\mathbf{Z}^{-1}(n) \quad (20)$$

and is then used together with the true measurements to update the states and estimate the covariance of the states as follow

$$\hat{\mathbf{s}}(n) = \hat{\mathbf{s}}^-(n) + \mathbf{K}(n)(\mathbf{z}(n) - \bar{\mathbf{z}}(n)) \quad (21)$$

$$\mathbf{P}(n) = \mathbf{P}^-(n) - \mathbf{K}(n)\mathbf{J}(n). \quad (22)$$

3.4.3 State augmentation of laser offsets

The rear and front laser have angular offsets $\phi_R(n)$ and $\phi_F(n)$ respectively. To estimate the laser offset they are added as states to form an augmented state vector $\mathbf{s}_a(n) = [x(n) \quad y(n) \quad \theta(n) \quad \gamma(n) \quad \phi_R(n) \quad \phi_F(n)]^T$. In the state space model Eq. (1) $\phi_R(n)$ and $\phi_F(n)$ are now modelled as constants with an uncertainty modelled as white noise. The uncertainty is used in the UKF to make them converge to their true value. Convergence time and variance of the offset estimates is adjusted by the size of the variances $\sigma^2_{\phi_R}$ and $\sigma^2_{\phi_F}$ of the white noises.

After augmentation the input vector is

$\mathbf{u}(n) = \begin{bmatrix} v(n) & \omega(n) & 0 & 0 \end{bmatrix}^T$ and the noise vector is again

$\mathbf{v}(n) \sim N(\mathbf{0}, \mathbf{Q})$

but with covariance

$$\mathbf{Q} = \begin{bmatrix} \sigma_v^2 & 0 & 0 & 0 \\ 0 & \sigma_\omega^2 & 0 & 0 \\ 0 & 0 & \sigma_{\phi_R}^2 & 0 \\ 0 & 0 & 0 & \sigma_{\phi_F}^2 \end{bmatrix}.$$

The input matrix changes into

$$\mathbf{\Gamma}_a(\mathbf{s}(n)) = \begin{bmatrix} \cos\theta(n) & 0 & 0 & 0 \\ \sin\theta(n) & 0 & 0 & 0 \\ \dfrac{-\sin\gamma(n)}{l_F\cos\gamma(n)+l_R} & \dfrac{-l_R}{l_F\cos\gamma(n)+l_R} & 0 & 0 \\ 0 & 1 & 0 & 0 \\ 0 & 0 & 1 & 0 \\ 0 & 0 & 0 & 1 \end{bmatrix}.$$

But the state matrix $\mathbf{\Phi}_s$ is still an identity matrix and the linearization becomes

$$\mathbf{H}_s(\mathbf{s}(n-1)) =$$

$$= \begin{bmatrix} 1 & 0 & -v(n)\sin(\theta(n)) & 0 & 0 & 0 \\ 0 & 1 & v(n)\cos(\theta(n)) & 0 & 0 & 0 \\ 0 & 0 & 1 & \dfrac{-l_R v(n)\cos(\gamma(n-1)) - v(n)l_F}{(l_R + l_F\cos(\gamma(n-1)))^2} & \dfrac{-\omega(n)l_R l_F \sin(\gamma(n-1))}{(l_R + l_F\cos(\gamma(n-1)))^2} & 0 & 0 \\ 0 & 0 & 0 & 1 & 0 & 0 \\ 0 & 0 & 0 & 0 & 1 & 0 \\ 0 & 0 & 0 & 0 & 0 & 1 \end{bmatrix}$$

Finally the initial covariance matrix $\mathbf{P}(0)$ change into

$$\mathbf{P}(0) = \begin{bmatrix} \sigma^2_{x_{init}} & & & & & \\ & \sigma^2_{y_{init}} & & & 0 & \\ & & \sigma^2_{\theta_{init}} & & & \\ & & & \sigma^2_{\gamma_{init}} & & \\ & 0 & & & \sigma^2_{\phi_{Rinit}} & \\ & & & & & \sigma^2_{\phi_{Finit}} \end{bmatrix}.$$

3.4.4 SLAM

The UKF needs a map to be able to estimate ϕ_R and ϕ_F but the mapping procedure in Chapter 3.4.1 is affected by ϕ_R and ϕ_F because of that can't the map be created before the offsets are estimated. It needs to be done simultaneously.

The map **M** could be created by adding laser scan information $\boldsymbol{z}(n)$ to **M** at each sample n using $\hat{\mathbf{s}}_a(n)$, estimated from Kalman filtering using artificial measurements $\tilde{\mathbf{Z}}(n)$ on **M** at n-1. This method has some drawbacks, one being that earlier estimates of ϕ_R and ϕ_F affects $\tilde{\mathbf{Z}}(n)$ and experiments showed that this made the Kalman filter unable to make ϕ_R and ϕ_F converge to their true values. It's solved by recreating the map around the machine at sample n from scratch for each setup of ϕ_R and ϕ_F in $\tilde{\mathbf{S}}(n)$. To recreate the map ray tracing is used in each old pose in $\hat{\mathbf{s}}_a(n+n_{\min us})$ with scan $\mathbf{z}(n+n_{minus})$, where n_{minus}= -$n_{step,}$ -2n_{step},…, -N_{minus} and n_{step} is the updating step used to decrease computation time.

Another drawback is that the map is less updated in the driving direction. This is solved by using the EKF to estimate future states $\hat{\mathbf{s}}_a^-(n+n_{pozitive})$, where $n_{positive}$=$n_{step,}$ 2n_{step} …, $N_{positive.}$ The poses in $\hat{\mathbf{s}}_a^-(n+n_{pozitive})$ are then used together with the laser scans $\boldsymbol{z}(n+n_{positive})$ to add data to the recreated map for each sigma setup in $\tilde{\mathbf{S}}(n)$ of ϕ_R and ϕ_F. This works over short travelled distances given that the model is correct.

Each ray tracing to a point on the map overwrites the old value. So the update order is of importance. The start position of the machine is exactly known when mapping, because we decide its coordinates. Poses in negative time are also more accurate because of that they have been estimated using the whole Kalman filter. For this reason it is more convenient to start with mapping in the future poses and end with mapping in the negative poses.

To get a more stable final output value the mean of the laser angle estimates $\hat{\phi}_R$ and $\hat{\phi}_F$ in $\hat{\mathbf{s}}_a(n)$ from samples at $n>N_{SM}$ are used to get $\bar{\phi}_R$ and $\bar{\phi}_F$. The first N_{SM} samples is skipped to give the estimated offsets time to settle because it

takes some time for the Kalman filter to make them converge to the true value. The reason to using the mean is that the Kalman filter put more weight in new information than old and thus can make $\hat{\phi}_R$ and $\hat{\phi}_F$ deviate because of bad new information. This could be helped with lower σ_{ϕ_F} and σ_{ϕ_R}, but then it converges to slow and/or gets stuck because of local minimas in the search space.

The final algorithm is:

Create a state matrix for old states $\mathbf{s}_{\text{old}}$
loop over all samples n
predict state $\hat{\mathbf{s}}_a^-(n)$ Eq. (14)
    calculate covariance $\mathbf{P}^-(n)$ Eq. (15)
    calculate sigma-points $\tilde{\mathbf{S}}(n)$ Eq. (16)
    loop over the $2N+1$ columns of $\tilde{\mathbf{S}}(n,p)$ using index p
        Allocate a clean map $\mathbf{M}$
        Allocate a temporary Nx $N_{positive}/n_{step}$ state matrix $\mathbf{s}_{\text{states}}$
        Allocate a temporary state vector $\mathbf{s}_{\text{vector}}=\tilde{\mathbf{S}}(n,p)$
        loop from 1 to $N_{positive}$ using index i
            predict state $\mathbf{s}_{\text{vector}}(n+i)$ Eq. (14)
            $\mathbf{s}_{\text{states}}(i)=\mathbf{s}_{\text{vector}}$
        end loop
        loop from $N_{positive}$ to 1 step $-n_{step}$ using index i
            update $\mathbf{M}$ at $\mathbf{s}_{\text{states}}(i)$ using ϕ_R and ϕ_F in $\tilde{\mathbf{S}}(n,p)$
        end loop
        loop from -1 to $-N_{negative}$ step $-n_{\text{step}}$ using index i
            update $\mathbf{M}$ at $\mathbf{s}_{\text{old}}(n+i)$ using ϕ_R and ϕ_F in $\tilde{\mathbf{S}}(n,p)$
        end loop
        ray trace in $\mathbf{M}$ at $\tilde{\mathbf{S}}(n,p)$ to get $\tilde{\mathbf{Z}}(n,p)$
    end loop
    calculate $\bar{\mathbf{z}}(n)$, $\mathbf{Z}(n)$, $\mathbf{J}(n)$, $\mathbf{K}(n)$ Eq. (17)(18)(19)(20)
    filter to get $\hat{\mathbf{s}}_a(n)$ Eq. (21)
    calculate covariance $\mathbf{P}(n)$ Eq. (22)
    $\mathbf{s}_{\text{old}}(n)=\hat{\mathbf{s}}_a(n)$
    if $n > N_{StartMean}$

$$\bar{\phi}_R = \bar{\phi}_R + \frac{\hat{\phi}_R - \bar{\phi}_R}{n - N_{SM}}$$

$$\bar{\phi}_F = \bar{\phi}_F + \frac{\hat{\phi}_F - \bar{\phi}_F}{n - N_{SM}}$$

    end if
end loop

3.5 Implementation

Laser and hinge angle offset estimation is made offline using a log-file containing all necessary data. The log file is recorded when the vehicle is driven a certain distance at a certain speed. To be able to create log-files, to test different laser offsets, an at Atlas Copco already existing SIMULINK simulator was modified. It simulated the kinematics of the ST14 seen in Eq. (3), the sensors and the laser scanning. Laser scans were originally made on maps created using lines but was modified to also handle grid maps. The laser simulation was also modified to include the laser spot effect discussed above so that the final simulator was able to simulate all errors in the laser sensor. Noises in the other sensors were skipped to decrease the complexity. The grid maps used were created using Profiling from real logs. The Route Profiling was together with the Simulated Playback, described in Chapter 3.4.1, already implemented by Atlas Copco in C++ and ready to use.

The hinge angle offset estimation and error propagation together with the measurement statistics in Chapter 3.3 were all implemented in MATLAB. As input to the hinge angle offset estimation method a real log-file was used. A script was also made to be able to go through a number of log-files to analyse the confidence interval of the method using the measurement statistics in Chapter 3.3.4.

All laser offset estimation parts in Chapter 3.4 were implemented in C++ using Microsoft Visual Studio 2005 and used data in a log-file together with a configuration file with all parameters as input. The laser offset implementation was built on modifications of an already existing Route Profiling and Playback code. From the C++ programs mat-files were delivered that could be analysed by MATLAB. A script was written in MATLAB to be able to automatically run estimations from many log-files automatically.

4 Error propagation in the hinge angle method

To see how the errors propagated through the hinge angle offset estimation two analyses were made using the error propagation in Chapter 3.3.3. The analyses shows how the unbiased angular speed measurement $\hat{\dot{\theta}}_{ubm}(n)$, speed measurement $v_m(n)$ and hinge angle measurement $\gamma_m(n)$ affects the standard deviation of the estimated offset $\hat{\sigma}_{\hat{\gamma}_o}$. A third analysis was made to see the effect of just iterating the hinge angle estimation ones using $\gamma_m(n)$ as the estimated hinge angle $\hat{\gamma}(n)$ in Eq. (7).

4.1 Analysis setup

All analyses were made at the systems sample frequency f_s of 25 Hz. An early analysis shown that the error isn't affected by $\dot{\gamma}_m(n)$ when smaller than 14 ^{o}/s, which is maximum steering speed, so no further analysis for it was made. In all

experiments $\gamma_m(n)$ was swept from 0 to 45°, where 45° is the maximum steer angle. $\hat{\dot{\theta}}_{ubm}(n)$ was calculated from Eq. (1) using $v_m(n)$ and $\gamma_m(n)$ as inputs. $\hat{\dot{\theta}}_{ubm}(n)$, $v_m(n)$ and $\gamma_m(n)$ were then inserted to the error propagation equations to give $\sigma_{\hat{\gamma}_o}$.

Different analyses were made starting with investigating how the standard deviation behaved when only using one sample at different speeds $v_m(n)$ equal to {1; 2.5; 4.5} m/s. Using more samples N only decrease $\hat{\sigma}_{\hat{\gamma}_o}$ with one divided by the square root of N and doesn't change the characteristic.

When travelling at low speed more samples N are collected compared to travelling at high speed. It was investigated how this affected $\hat{\sigma}_{\hat{\gamma}_o}$ using Eq. (11) at the speeds $v_m(n)$ equal to {1; 2.5; 4.5} m/s when travelling 50 m.

A final analysis was made to evaluate the error in $\hat{\gamma}_o$ from using $\gamma_m(n)$, including the offset γ_o, as the estimated hinge angle $\hat{\gamma}(n)$ in the denominator of Eq. (7) and iterate the hinge angle estimation method only one time. It should be noticed that the error is a constant error that depends on γ_o and not a random error as those above. Here $\dot{\gamma}(n)$ affects the error and according to Eq. (7) does larger $\dot{\gamma}(n)$ give larger effects, so $\dot{\gamma}(n)$ was put to its absolute maximum value of 14 °/s. The error also increase with decreased speed so to find the maximum error the speed was put to the lowest speed used around 1.0 m/s.

Increased offset also increases the error according to Eq. (7). To see the effect of different offsets γ_o, the set {2, 5, 25, 45}° was tested.

4.2 Results

Using only one sample to estimate the offset gives the standard deviation $\hat{\sigma}_{\hat{\gamma}_o}$ seen in Figure 4 at different hinge angles $\gamma_m(n)$ and speeds $v_m(n)$. As seen $\hat{\sigma}_{\hat{\gamma}_o}$ increases with $\gamma_m(n)$ and decreases with increased speed $v_m(n)$.

The result for travelling 50 m, giving different number of samples, can be seen in Figure 5. As seen in the figure $\hat{\sigma}_{\hat{\gamma}_o}$ increase less for large angles and low speeds compared with Figure 4.

Analyses of the effects of using $\gamma_m(n)$ as $\hat{\gamma}(n)$ in Eq. (7) showed that the error in $\hat{\gamma}_o$ increased almost linearly with increased $\gamma_m(n)$ as seen in Figure 6. It could also be seen that the error in $\hat{\gamma}_o$ is always smaller then the true offset.

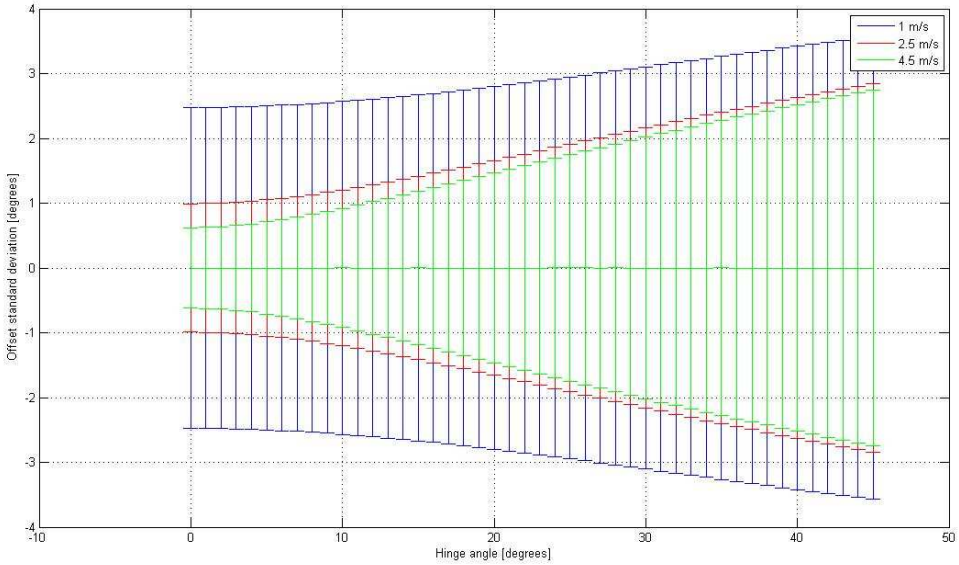

Figure 4: The estimated standard deviation $\hat{\sigma}_{\hat{\gamma}_o}$ of the hinge angle offset at one sample of $v_m(n)$ equal to {1; 2.5; 4.5} m/s, $\gamma_m(n)$ equal to [0 45]^o and $\hat{\dot{\theta}}_{ubm}(n)$, calculated using Eq. (1). It should be observed that $\hat{\sigma}_{\hat{\gamma}_o}$ increases with decreased $v_m(n)$ and increased $\gamma_m(n)$.

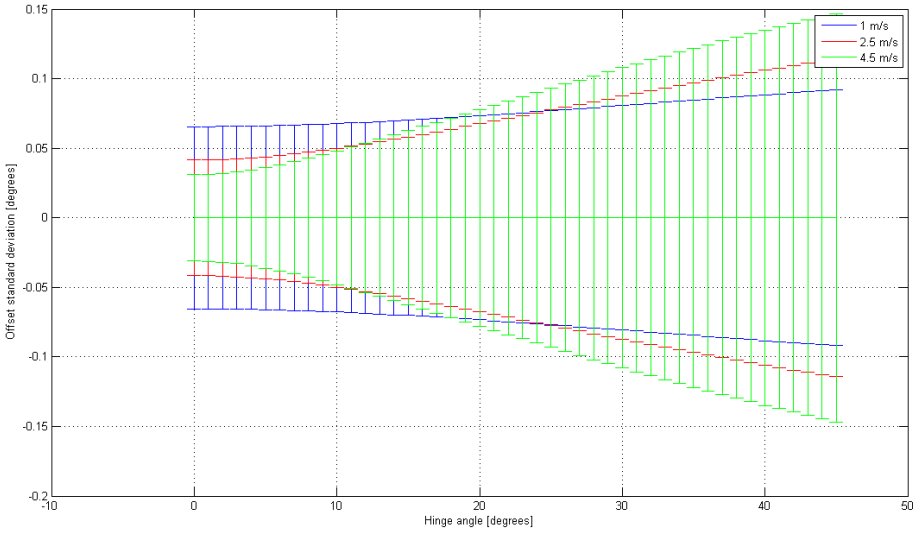

Figure 5: $\hat{\sigma}_{\hat{\gamma}_o}$ after sampling with f_s and travelling 50 m. $v_m(n)$ is equal to {1; 2.5; 4.5} m/s and $\gamma_m(n)$ is equal to [0 45]^o. It should be observed that $\hat{\sigma}_{\hat{\gamma}_o}$ increases with decreased $v_m(n)$ and increased $\gamma_m(n)$ but less at low speeds. From the figure, it is clear that for small angles at speed 2.5 m/s and above we are able to estimate the offset within ± 0.2^o with 99 % confidence (2.576 $\sigma_{\hat{\gamma}_o}$ < 0.2^o).

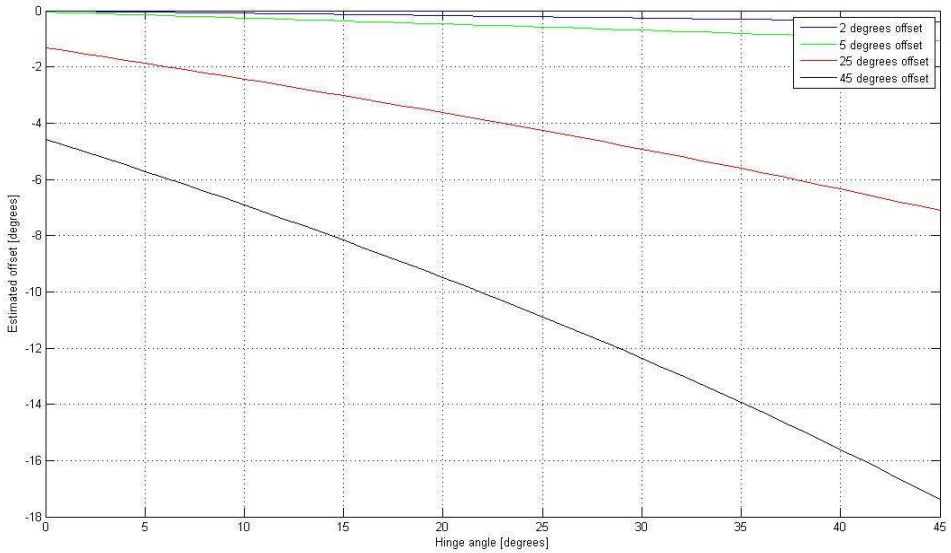

Figure 6: Error in estimated offset at the known offsets {2, 5, 25, 45}^{o} because of using $\gamma_m(n)$ as $\hat{\gamma}(n)$ in Eq. (7). It should be observed that the error is always less than the true offset.

4.3 Discussion

From Figure 4 and Figure 5 it can be concluded that the estimated standard deviation $\hat{\sigma}_{\hat{\gamma}_o}$ increases with increased hinge angle $\gamma_m(n)$ and decreases with increased speed $v_m(n)$. The reason for increased $\hat{\sigma}_{\hat{\gamma}_o}$ with increased $\gamma_m(n)$ is because of that uncertainty in speed increases the uncertainty in rotation speed $\dot{\theta}$ with increased $\gamma_m(n)$. If the uncertainty in speed is zero then $\hat{\sigma}_{\hat{\gamma}_o}$ is almost constant for increased $\gamma_m(n)$. Increasing $v_m(n)$ gives increased $\dot{\theta}$ when keeping $\gamma_m(n)$ constant and thereby better readings. It should also be remembered that according to Eq. (11) increasing the sample size N by driving a longer distance decreases $\hat{\sigma}_{\hat{\gamma}_o}$. From Figure 5 it could be concluded that when driving 50 m the 99 % confidence interval $2.576\sigma_{\hat{\gamma}_o}$ is only 0.21^{o} even for low speeds at small $\gamma_m(n)$, which is close to $\pm 0.2^{o}$.

When analysing the error introduced because of using $\gamma_m(n)$ as $\hat{\gamma}(n)$ in Eq. (7) it was found that the error increased almost linearly with $\gamma_m(n)$. It was also found that the error in $\hat{\gamma}_o$ was always smaller than the true offset which makes it possible to iterate to find the best estimate $\hat{\gamma}_o$ of the true hinge angle. The error is a constant error, which means that taking more samples doesn't help, but iterating as described in Chapter 3.3.1 reduces the error to zero.

A conclusion is that because of increased $\hat{\sigma}_{\hat{\gamma}_o}$ at high hinge angles it's expected that the machine is going to be driven as straight as possible. When using the mean of $\gamma_m(n)$ as an first approximation of the offset this gives a remaining offset in the hinge angle estimate $\hat{\gamma}(n)$ equal to the mean of the hinge angle $\gamma(n)$, see Eq. (8). If $\gamma(n)$ is small the error is even smaller according to Figure 6 so as long as the machine is not driven with to high $\gamma(n)$ no iteration is needed.

5 Hinge angle experiments

To test the calibration method a series of experiments were needed. A list of goals below was created to fully test the systems limits.

- Find the minimum length needed to get good enough precision.
- Check the precision in relation to speed. Find minimum speed.
- Check the precision in relation to turn radius. Find maximum angle.
- Check the deadband of the machine.
- See if stretching the machine in one direction gives better performance.

45 experiments to achieve these goals were put up. In most of them one drove straight or in an arc. No experiment was made with a large hinge angle offset because the theoretical analysis above proves that it doesn't work.

The experiments were made on an ST14 LHD in an old underground mine in Kvarntorp in Kumla by an experienced driver. The data were then saved analysed offline in MATLAB. The third goal couldn't be tested because of limited space in the mine drift.

5.1 Experiment setup

All experiments were repeated at the speeds {1.2; 2.5; 4.5} m/s because they are the maximum speeds at each gear and thereby easy to keep constant. In all cases the driver tried to drive relaxed so normal correction oscillations should be included. The hinge angle sensor was pre-calibrated to give a reasonable hinge angle. Then the mean of the sampled hinge angles when driving straight 300 m was calculated, which gave the remaining true hinge angle offset with a precision of around $\pm 0.05^{\circ}$. The true offset was then used as a reference in the experiments. To get the gyro bias the machine stood still for 10 s before and after completing a run through the drift to collect gyro bias data.

The first experiments were made to test the method under normal conditions. To collect data the machine was driven straight one to two times back and forth through a 300 m long tunnel at the different speeds. A straight path was chosen because that should give the smallest errors.

To test the last two goals the machine was driven with the true hinge angles of $\{0.2; \pm 0.7\}^{\circ}$ at different speeds a distance of 100 m in an 11 m wide tunnel. The

hinge angle of 0.2^o was chosen to see if better performance was achieved if the machine was stretched in one direction. The thought was that if one stretches the machine in one direction the machine should not oscillate because of the play in the axles and the hinge. This then should increase the performance of the method. $\pm 0.7^o$ were chosen to see if there was any play in the hinge angle sensing and thereby different results in the offset estimation.

The reason to not test with random moves was that the errors arise when the angle is high and/or speed low. Also the error that comes from increasing/decreasing the angle is small. If totally random moves had been made the errors had cancelled out.

Enough with data were collected at each setup to be able to divide it into a number of partions containing N_2 measurements, where N_2 was chosen to 250, 500 and 1000 samples, to test the precision at different lengths. Each experiment setup was repeated N_1 times to find the confidence interval of the estimated offsets.

A number of statistics were then calculated using the data starting with the mean $\bar{\hat{\gamma}}_o$ of all N_1 offset estimates $\hat{\gamma}_o$ to see that they were centred on the true offset. Then the maximum deviation from the true offset $d_{\hat{\gamma}_o \max}$ was calculated for each experiment setup. $d_{\hat{\gamma}_o \max}$ is the maximum error from our measurements, which is only a small amount of the whole population. Confidence intervals take the whole population into consideration and are more assertive statistics. The methods described in Chapter 3.3.3 and 3.3.4 were therefore used to find different 99 % confidence intervals for $\hat{\gamma}_o$. For each measurement *n* in experiment *p* the 99 % confidence interval was calculated using the error propagation with the measurements as input. The largest confidence interval $z_{0.99} \max(\hat{\sigma}_{\hat{\gamma}_o}(p))$, where $z_{0.99}$ =2.576, was then recorded for each setup.

The largest and smallest confidence interval $z_{0.99} \max(\sigma_{\hat{\gamma}_o 1}(p))$ respectively $z_{0.99} \min(\sigma_{\hat{\gamma}_o 1}(p))$, using the standard deviation in each experiment *p*, were recorded for each setup. By using the estimated standard deviation $s_{\hat{\gamma}_o}$ of all the $\hat{\gamma}_o$:s, the confidence interval with lower boarder $z_{0.99} L_1$ and higher boarder $z_{0.99} L_2$ was calculated and recorded for each setup together with the estimated confidence interval $z_{0.99} s_{\hat{\gamma}_o}$ and the mean of all N_1 ratios $\frac{\chi^2}{N_1 - 1}$ for each experiment setup.

5.2 Results

From the mean value, when driving 300 m straight, it was found that the true remaining hinge angle was 0.31 ^{o} ±0.05 ^{o}. So the goal for the experiments is to get hinge angle offsets in the range 0.31 ^{o} ±0.20 ^{o}, to show that the method can operate under all conditions.

5.2.1 Driving straight

Table 1: (a) The experiment setups, mean hinge offsets $\bar{\hat{\gamma}}_o$ and maximum deviating offsets $d_{\hat{\gamma}_o \max}$ when driving with a true hinge angle γ of 0^{o}. (b) The Gaussian 99 % confidence intervals for the experiments using different methods.

a.

Exp. Setup	γ [^{o}]	Gear	v [m/s]	N_2	f_s	Distance	N_1	$\bar{\hat{\gamma}}_o$	$d_{\hat{\gamma}_o \max}$
1	0	1	1.3	250	20	16.25	19	0.34	0.36
2	0	2	2.6	250	20	32.50	38	0.30	0.20
3	0	3	4.5	250	20	56.25	38	0.32	0.15
4	0	1	1.3	500	20	32.50	9	0.34	0.20
5	0	2	2.6	500	20	65.00	18	0.30	0.11
6	0	3	4.5	500	20	112.50	18	0.32	0.11
7	0	1	1.3	1000	20	65.00	4	0.34	0.19
8	0	2	2.6	1000	20	130.00	6	0.30	0.05
9	0	3	4.5	1000	20	225.00	6	0.31	0.05

b.

Exp. Setup	$z_{0.99}\max(\hat{\sigma}_{\hat{\gamma}_o}(p))$	$z_{0.99}\min(\sigma_{\hat{\gamma}_o 1}(p))$	$z_{0.99}\max(\sigma_{\hat{\gamma}_o 1}(p))$	$z_{0.99}L_1$	$z_{0.99}s_{\hat{\gamma}_o}$	$z_{0.99}L_2$	$\frac{\bar{\chi}^2}{N_1-1}(p)$
1	0.26	0.08	0.20	0.20	0.29	0.49	6.40
2	0.13	0.06	0.19	0.14	0.19	0.26	5.39
3	0.08	0.04	0.19	0.12	0.15	0.21	7.94
4	0.19	0.07	0.11	0.15	0.25	0.60	9.47
5	0.10	0.04	0.13	0.10	0.14	0.23	4.06
6	0.06	0.03	0.12	0.08	0.11	0.19	9.88
7	0.13	0.05	0.07	0.14	0.28	1.79	23.23
8	0.07	0.03	0.06	0.03	0.06	0.24	2.61
9	0.04	0.03	0.06	0.04	0.07	0.25	7.30

The results from driving straight with different speeds and using different number of samples can be seen in Table 1, for figures see appendix B. As seen, the estimated offsets $\hat{\gamma}_o$ have a mean $\bar{\hat{\gamma}}_o$ very close to 0.31^{o} in all cases. If one looks at their distributions one finds out that they have Gaussian distributions which tell us that our assumptions made in Chapter 3.3.3 and 3.3.4 are valid. From Table 1 it could be seen that for all cases, besides the one when only using 250 samples and driving with the first gear, $d_{\hat{\gamma}_o \max}$ is smaller than or equal to 0.20^{o}.

Using gear 2 and 3 instead of gear 1 largely improves the performance according to $d_{\hat{\gamma}_o \max}$. Also increasing the distance driven and thereby the sample size decreases $d_{\hat{\gamma}_o \max}$ for gear 2 and 3 but only a small amount for gear 1 at larger sample sizes. The difference between using gear 2 and 3 decreases with increased sample size.

Table 1b shows the positive borders of different 99 % confidence intervals calculated using the methods in Chapter 3.3.3 and 3.3.4. $z_{0.99}L_1$ and $z_{0.99}L_2$ tell in which interval the true positive confidence interval border is. They only relies on that the measurements are Gaussian and are therefore the most reliable ones. $z_{0.99} \max(\hat{\sigma}_{\hat{\gamma}_o}(p))$ is the most uncertain statistic. As seen in Table 1b it compared to $z_{0.99}L_1$ underestimates the confidence interval in most cases. $z_{0.99}\sigma_{\hat{\gamma}_o 1}(p)$ also underestimates the confidence interval sometimes because of that $z_{0.99} \min(\sigma_{\hat{\gamma}_o 1}(p))$ is smaller than $z_{0.99}L_1$ for all setups and sometimes leave reasonable estimates $z_{0.99} \max(\sigma_{\hat{\gamma}_o 1}(p))$, which in most cases are in the interval defined by $z_{0.99}L_1$ and $z_{0.99}L_2$. But on average it underestimate the confidence interval according to the mean of $\frac{\chi^2}{N_1 - 1}$.

It can be seen from $z_{0.99}s_{\hat{\gamma}_o}$ that using confidence intervals instead of $d_{\hat{\gamma}_o \max}$ gives similar results. By looking at $z_{0.99}L_2$ it can be seen that for gear 2 and gear 3 the error is smaller than 0.3^o in all cases if one includes the measurement error of the true offset. Increasing the distance travelled from 33 m doesn't improve $z_{0.99}L_2$. To see the spread of the offsets and their confidence intervals see appendix B.

5.2.2 Small turning

Table 2 (a) The experiment setups, mean hinge offsets $\bar{\hat{\gamma}}_o$ and maximum deviating offsets $d_{\hat{\gamma}_o \max}$ when driving with a true hinge angle γ of 0.2^o. (b) The Gaussian 99 % confidence intervals for the experiments using different methods

a.

Exp. Setup	γ [°]	Gear	v [m/s]	N_2	f_s	Distance	N_1	$\bar{\hat{\gamma}}_o$	$d_{\hat{\gamma}_o \max}$
10	0.2	1	1.3	250	25	13.00	12	0.30	0.25
11	0.2	2	2.6	250	25	26.00	12	0.27	0.18
12	0.2	3	4.5	250	25	45.00	12	0.37	0.25
13	0.2	1	1.3	500	25	26.00	4	0.29	0.13
14	0.2	2	2.6	500	25	52.00	4	0.28	0.05
15	0.2	3	4.5	500	25	90.00	4	0.39	0.18

b.

Exp. Setup	$z_{0.99}\max(\hat{\sigma}_{\hat{\gamma}_o}(p))$	$z_{0.99}\min(\sigma_{\hat{\gamma}_o 1}(p))$	$z_{0.99}\max(\sigma_{\hat{\gamma}_o 1}(p))$	$z_{0.99}L_1$	$z_{0.99}s_{\hat{\gamma}_o}$	$z_{0.99}L_2$	$\frac{\bar{\chi}^2}{N_1-1}(p)$
10	0.31	0.20	0.47	0.22	0.34	0.70	1.75
11	0.16	0.10	0.20	0.15	0.23	0.47	2.36
12	0.10	0.08	0.14	0.15	0.23	0.46	4.65
13	0.22	0.16	0.26	0.13	0.26	1.69	2.35
14	0.11	0.11	0.12	0.02	0.05	0.28	0.15
15	0.07	0.07	0.08	0.08	0.15	1.01	4.92

From Table 2 it can be seen that with high probability, by looking at $z_{0.99}L_1$ and $z_{0.99}s_{\hat{\gamma}_o}$, the performance has not improved when turning 0.2°. Instead it's possible that it has decreased, especially for gear 3. For gear 3 also the mean offset estimate $\bar{\hat{\gamma}}_o$ is unusually high both at a sample size of 250 and 500 samples. To see the spread of the offsets and their confidence intervals see appendix B.

5.2.3 Increased turning and deadband

Table 3: (a) The experiment setups, mean hinge offsets $\bar{\hat{\gamma}}_o$ and maximum deviating offsets $d_{\hat{\gamma}_o \max}$ when driving with a true hinge angle γ of ±0.7°. (b) The Gaussian 99 % confidence intervals for the experiments using different methods.

a.

Exp. Setup	γ [°]	Gear	v [m/s]	N2	fs	Distance	N1	$\bar{\hat{\gamma}}_o$	$d_{\hat{\gamma}_o \max}$
16	0.7	1	1.3	250	25	13.00	16	0.38	0.51
17	0.7	2	2.6	250	25	26.00	16	0.36	0.29
18	0.7	1	1.3	500	25	26.00	8	0.39	0.45
19	0.7	2	2.6	500	25	52.00	8	0.37	0.19
20	-0.7	1	1.3	250	25	13.00	10	0.17	0.47
21	-0.7	2	2.6	250	25	26.00	10	0.25	0.32
22	-0.7	1	1.3	500	25	26.00	4	0.19	0.24
23	-0.7	2	2.6	500	25	52.00	4	0.24	0.13

b.

Exp. Setup	$z_{0.99}\max(\hat{\sigma}_{\hat{\gamma}_o}(p))$	$z_{0.99}\min(\sigma_{\hat{\gamma}_o 1}(p))$	$z_{0.99}\max(\sigma_{\hat{\gamma}_o 1}(p))$	$z_{0.99}L_1$	$z_{0.99}s_{\hat{\gamma}_o}$	$z_{0.99}L_2$	$\frac{\bar{\chi}^2}{N_1-1}(p)$
16	0.31	0.19	0.44	0.36	0.53	0.95	4.31
17	0.16	0.10	0.24	0.28	0.41	0.73	8.15
18	0.22	0.15	0.26	0.26	0.45	1.18	5.60
19	0.11	0.09	0.15	0.11	0.18	0.47	3.30
20	0.31	0.25	0.45	0.31	0.50	1.14	2.17
21	0.16	0.11	0.17	0.18	0.29	0.65	4.32
22	0.22	0.21	0.26	0.16	0.32	2.01	1.94
23	0.11	0.10	0.11	0.06	0.12	0.74	1.34

By looking at the $\bar{\hat{\gamma}}_o$ at ±0.7° in Table 3 it's found that turning positive increases the estimated hinge angle $\hat{\gamma}_o$ and turning negative decreases $\hat{\gamma}_o$. It could also be seen that the deviation from the true hinge angle offset decreases with speed. If Table 2 and Table 3 are compared it can also be observed that increased turning also increases the deviation in $\hat{\gamma}_o$. One exception is at gear 3 in Table 2 where the deviation is equally large as those at other gears in Table 3. To see the spread of the offsets and their confidence intervals see appendix B.

5.3 Discussion

From the results when driving straight one can draw the following conclusions:

1. Performance improves with higher speed and longer distance.
2. The difference of using gear 3 and 2 decreases with distances travelled.
3. Driving slower than 2.5 m/s and shorter than 33 m is not recommended.

As seen in Table 1 both $z_{0.99}\hat{\sigma}_{\hat{\gamma}_o}(p)$ and $z_{0.99}\sigma_{\hat{\gamma}_o 1}(p)$ are underestimating the true confidence interval. One of the reasons for $z_{0.99}\hat{\sigma}_{\hat{\gamma}_o}(p)$ to underestimate the confidence interval is that it uses a model, which in reality always contains model errors. It also only takes into consideration the standard deviations of the sensors that for the speed and the gyro contain modelling errors. Errors like slippage and vibrations, which affects the gyro, is also not considered. Even when $z_{0.99}\hat{\sigma}_{\hat{\gamma}_o}(p)$ underestimates the confidence interval it still models the behaviour correctly, when compared to $z_{0.99}s_{\hat{\gamma}_o}$ in Tables 1, 2 and 3.

Driving at 4.5 m/s didn't give any significant improvement in both the straight case and when a small turn was made. It gave the same confidence interval, driving 56 m at 4.5 m/s, as driving 65 m at 2.5 m/s, as seen in Table 1. Driving slower makes it easier to perform the calibration in small and narrow mines so 2.5 m/s is preferred to 4.5 m/s.

$z_{0.99}\sigma_{\hat{\gamma}_o 1}(p)$ only rely on the facts that the measurements are not correlated, that the sample size is large and that they have a Gaussian distribution. The later has been confirmed and the sample size is large. By calculating the correlation it was found that there exists an oscillation with a period of around 1 s in the sample offsets. By looking at the gyro readings and the machine when the machine stops it has been seen that the LHD is swaying for some seconds with a period of 1 s. From this it can be concluded that the LHD has a swaying resonance frequency of around 1 s and because of the correlation the variance is under estimated. The error introduced by the swaying is small if large sample sizes are used.

The experiments made when turning with a small hinge angle shows that there is nothing gained in precision by doing it. It's even so that the precision seems to decrease according to Table 2. When using 500 samples and gear 2, Table 2,

it seems like that the confidence interval is largely decreased, but looking at $z_{0.99}L_2$ one understands that it is possible that it's underestimated. These results are also backed up by the mean ratio, which normally is larger than 1. The reason for the mean offset estimate $\bar{\hat{\gamma}}_o$ to be high at high speeds can't be explained by other than the occurrence of slippages at high speed when turning. This is probably also the reason for the increased confidence interval, but it should be remembered that there exists a uncertainty in $\bar{\hat{\gamma}}_o$.

Another conclusion is that when the turning is increased a deadband is created according to Table 3. It's not a normal mechanical deadband because it shouldn't increase with turning angle. More likely it appears because of slippages. It can also be observed from $z_{0.99}L_1$ and $z_{0.99}s_{\hat{\gamma}_o}$ in Table 1, 2 and 3 that the confidence interval and thereby the spread increases with increased hinge angle. From this a conclusion can be drawn that driving as straight as possible is recommended.

It should be noted that the $z_{0.99}L_1$ to $z_{0.99}L_2$ intervals are too large and overlapping, because of too few experiments with each setup, in order to with 99 % confidence assure the above conclusions. But there is a high probability that they are right. It should be remembered that $z_{0.99}L_1$ and $z_{0.99}L_2$ depends on the number of samples and therefore converges to the true confidence interval when the number of experiments with the same setup goes to infinity and vice versa. Without more data it can only be assured that the offset estimation error is less than $z_{0.99}L_2$. A effect of this can be seen in the straight case where it seems as increasing the distance doesn't decrease $z_{0.99}L_2$. This happens because the sample size decreases with distance. If one instead looks at the estimated confidence interval $z_{0.99}s_{\hat{\gamma}_o}$ it decreases. The problem of too few samples is also one of the factors that drives $z_{0.99}L_2$ high in the cases when making small turns.

From the above experiments it can be concluded that the method can deliver a hinge angle offset with a precision better than 0.3^o with a 99 % confidence as long as the machine is driven straight 33 m or longer at a speed of 2.5 m/s. The goal of 0.2^o can't be achieved following the criterions in Chapter 2.1 but it is possible, with high probability, that more experiments is going to show that the true 99 % confidence interval lies lower than the here estimated L_2:s.

Later investigations of the LHD used at data collection in Kvarntorp showed that a part in the hinge angle sensor was broken. This gave the hinge angle sensor a play. The load on the hinge angle changes when the machine goes in different directions which then probably affected its readings because of the play. This can have altered the results negatively and is probably the reason for the deadband.

6 Required laser offset accuracy

For the lasers the required accuracy was specified as a maximum scan matching error in the map. To be able to specify the corresponding required precision of the angular offset of the lasers a set of offsets in a number of environments were tested to find the ones giving the maximum allowed scan matching error of 0.35.

6.1 Analysis setup

To find the offsets giving the maximum allowed scan matching error a grid of varying laser offset combinations (ϕ_R, ϕ_F) was created. It was expected that the laser offsets never would be larger than $\pm 3^o$ degrees. But we chose to use a grid with the range $[-5\ 5]^o$ in each direction and a resolution of 1^o. The grid was applied on real log data from six different routes in a mine in the Finnish town Kemi. Three routes were straight and three routes had a turn. For each grid point and route the mapping and evaluation procedure described in Chapter 3.4.1 was applied using the offsets in the grid as correction. The reference offsets were estimated from the three straight routes using the above method with a resolution of 0.3^o and were found to be equal to $(-0.8;0.3)^o$, which then were represented by the vector $\boldsymbol{\varphi}_{ref}$.

6.2 Results

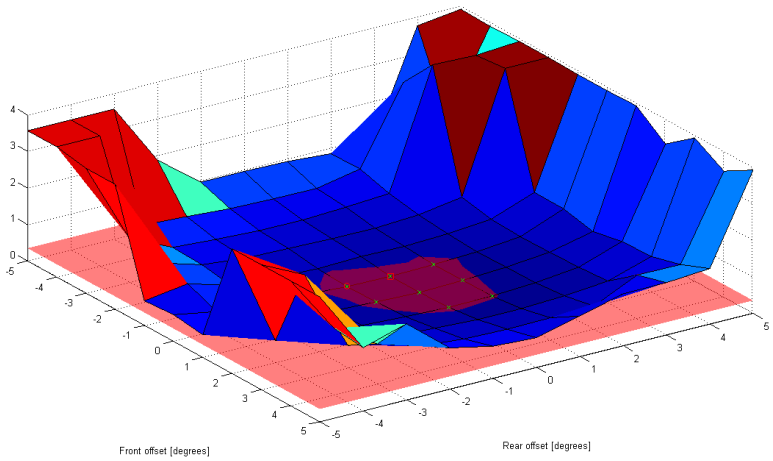

Figure 7: Highest scan matching error from all routes at each offset combination. Green crosses and the red shaded area in the middle show the offsets giving a ε_{match} smaller than 0.35. The red circle shows the offset $\boldsymbol{\varphi}_{ref}$ and the red square shows the offsets $\boldsymbol{\varphi}_{Goptima}$ with lowest ε_{match}.

Figure 7 shows the total maximum of the scan matching errors, when driving the paths with different offsets. The green crosses and the red shaded area in the middle show the offset combinations that give a ε_{match} smaller than 0.35 for all

paths. The red circle shows the offsets $\boldsymbol{\varphi}_{ref}$ closest to the reference offsets, where (ϕ_R, ϕ_F) is equal to (-0.8; 0.3)^o. As seen it doesn't lie in the middle of the allowed angles and nor do the offsets $\boldsymbol{\varphi}_{GOptima}$ with lowest ε_{match}, shown as a red square in (0.0;0.0)^o. It can also be seen that $\boldsymbol{\varphi}_{ref}$ doesn't coincide with $\boldsymbol{\varphi}_{GOptima}$ and that the allowed area based on the matching error criterion is just allowing the offsets to vary -0.5^o from their reference value $\boldsymbol{\varphi}_{ref}$.

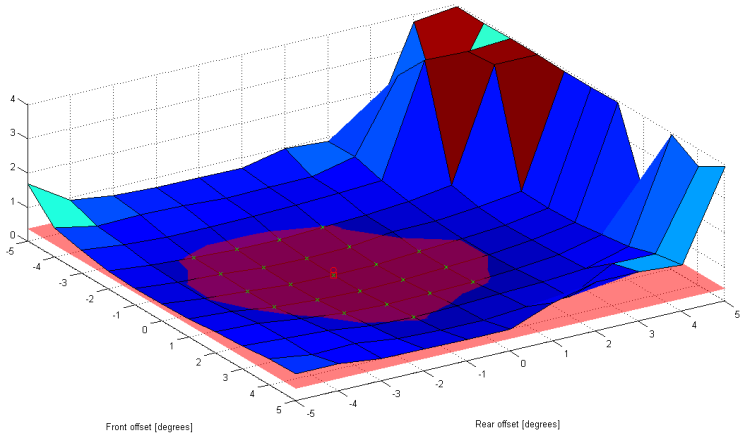

a

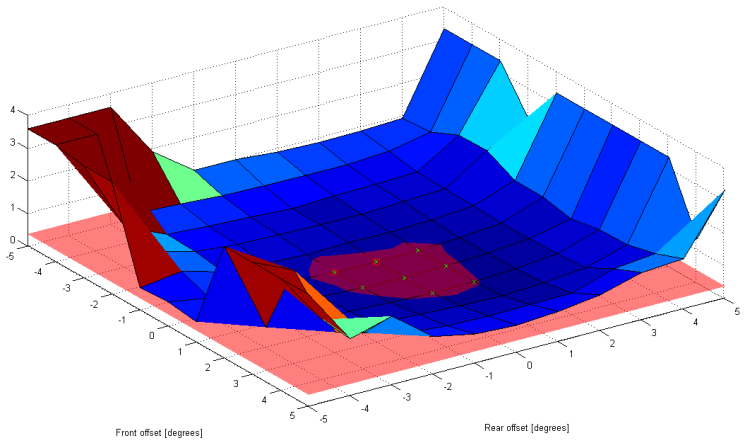

b

Figure 8: Maximum scan matching error from straight routes in a and routes with a turn in b. Green crosses and the red shaded area in the middle shows the offsets giving a ε_{match} smaller than 0.35. The red circle shows the offsets closest to the true offsets $\boldsymbol{\varphi}_{ref}$ and the red square in shows the offsets, $\boldsymbol{\varphi}_{SOptima}$ in a and $\boldsymbol{\varphi}_{TOptima}$ in b, with lowest ε_{match}.

In Figure 8a and 8b the maximum scan matching errors from straight paths respectively paths with a turn can be observed. Figure 8a from the straight paths shows that the offsets $\varphi_{SOptima}$ with lowest ε_{match} in the straight cases coincides with φ_{ref}. It also shows that the area of allowed offset is larger than in Figure 7, centred around φ_{ref} and allows the offset to vary $\pm 2^{o}$. These results are also valid if one looks at the three paths separately. It could be seen that Figure 8b from the turning paths resembles Figure 7 since it has a higher ε_{match} for almost all angles and thereby dominates Figure 7. It should however be mentioned that it's only one path that dominates the other three and decides the shape of Figure 7 and 8b. In all turning cases $\varphi_{TOptima}$ varied but the area of allowed offsets was centred around φ_{ref} and had the same size as in the straight cases with exception of the dominating one.

6.3 Discussion

It's the worst cases that set the limits because the scan match error must always stay under 0.35. From Figure 7 the conclusion can be drawn that the offsets can't be allowed to deviate more than -0.5^{o} from their true value. One also assumes that one can't allow them to deviate more than $+0.5^{o}$. This conclusion comes from the symmetry in the systems dimensions which should give symmetric scan matching errors and is confirmed by the straight cases where the allowed area is centred around φ_{true}. More cases had been needed to investigate this further but because of too large computation times as well as lack of relevant data this was not possible.

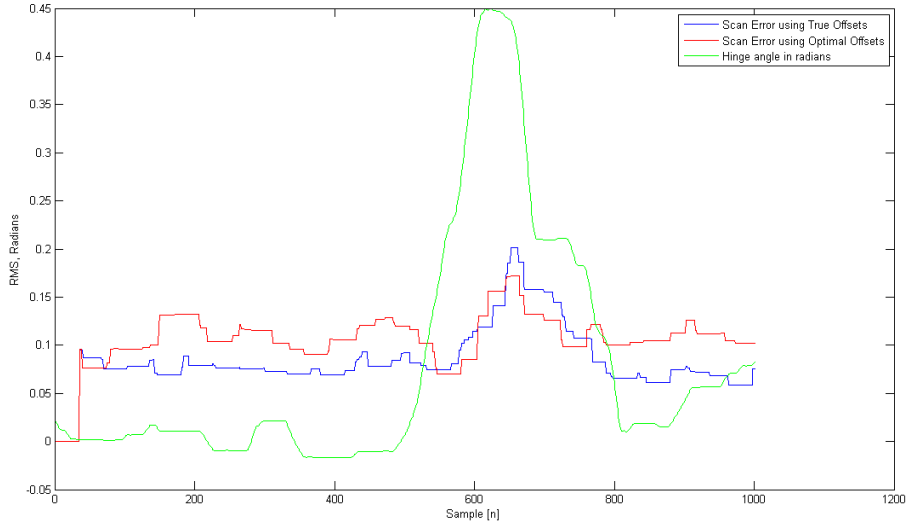

Figure 9: Data from one of the turning paths. As seen there exist an offset that gives a lower maximum scan matching error at the turn than the true offset.

The reason for $\boldsymbol{\varphi}_{TOptima}$ to sometimes deviate from $\boldsymbol{\varphi}_{ref}$ in the turning cases can be explained by Figure 9 showing data from one of the turning paths. In Figure 9 the blue line is ε_{match} using $\boldsymbol{\varphi}_{ref}$, the red line is ε_{match} using $\boldsymbol{\varphi}_{TOptima}$ and the green line is the hinge angle γ in radians. From the figures it can be observed that ε_{match} goes high when γ goes high. $\boldsymbol{\varphi}_{ref}$ gives a better ε_{match} on average but $\boldsymbol{\varphi}_{TOptima}$ gives the lowest maximum ε_{match}. One of the reasons for ε_{match} to increase in turns is because of the geometry of the mine drift and the side drift, which the turn is made into, because ε_{match} is also increasing when just passing a side drift, which can be seen by looking at ε_{match} for each sample in the straight cases.

Sometimes there are also walls with ventilation tubes or cable ladders that make the laser data corrupt and increase ε_{match}. ε_{match} also goes down at erroneous offsets because of above mentioned reasons. As a result of that we didn't collect the data ourselves, we can't know where there were things interfering with our measurement. Nevertheless, non true offsets have shown to sometimes give better scan matching errors.

7 Accuracy of the laser offset estimation

To evaluate that the method provide reliable offsets with high enough precision a set of experiments were performed on real and simulated data.

7.1 Test setup

Table 4: Places, angles used at simulation and number of real tests at each location.

	Simulated (ϕ_R;ϕ_F) [°]	Real [number of tests]
Kemi Straight	(0,0), (0,3), (3,3)	10
Kemi Turn	(0,0), (0,3), (3,3)	3
Kvarntorp	(0,0), (0,3), (3,3)	5

A test schema seen in Table 4 was created with different conditions to test. It contains tests to see if the method could handle both straight and turning paths in real and simulated cases. The tests were done using log-files from a mine in Kemi, which has representable proportions. The simulation tests were made to see that the method could handle all expected offsets ϕ_R and ϕ_F because we couldn't do real experiments where we turned the lasers. Routes from the same area in Kvarntorp were used to test how it handled large mine drifts with many side drifts. It was also of interest to see how fast it converged in the different cases and how long driving distance that was needed.

The method shouldn't need reconfiguration for each environment so in all tests the same parameter configuration was used. A speed of around 2.5 m/s was used because the early tests had shown that higher speeds gave the best result and 2.5 m/s is the maximum usable speed. The hinge angles measurements of

the real data where compensated for sensor offset using the method described in Chapter 3.3.1. In the simulations the same driving path was used in each location for all offsets to not affect the results. 4^o turns were made in the end of the Kvarntorp runs to see if the Kalman filter could handle it.

When analysing the real paths the true offsets were known for the Kemi data from the analysis above and equal to $(-0.8;0.3)^o$. In Kvarntorp the true offsets weren't known but constant in all routes. The reason to use real cases was to be able to analyse the accuracy under real circumstances. In the straight Kemi cases 10 different log-files had been recorded in parts of two areas in the mine.

As a result of this the following tests are in the same areas

- 1, 3, 4 and 8
- 6, 9 and 2
- 7, 10 and beginning of 5

The Kalman filter uses the scan matching error ε_{match} to update its estimates and a larger ε_{match} makes the algorithm to converge faster. As seen in Figure 7 equal offsets and opposite offsets give almost the same scan matching error ε_{match}. If (ϕ_R, ϕ_F) are $(3,0)^o$ or $(0,3)^o$ it should be harder than if they are $(3,3)^o$ to find them, due to lower scan ε_{match}. But the convergence shouldn't depend on if the offsets are $(3,0)^o$ or $(0,3)^o$. From this a conclusion was drawn that it's enough to test with the offsets (ϕ_R, ϕ_F) equal to $\{(0,0)\ (0,3)\ (3,3)\}^o$.

7.2 Results

7.2.1 Driving straight in a normal mine drift

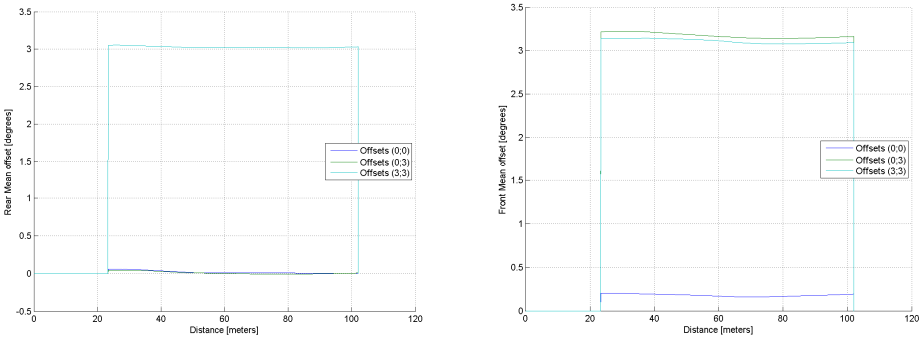

$\bar{\phi}_R$ $\bar{\phi}_F$

Figure 10: $\bar{\phi}_R$ and $\bar{\phi}_F$ from the simulated straight path in Kemi at laser offsets $\{(0,0)\ (0,3)\ (3,3)\}^o$.

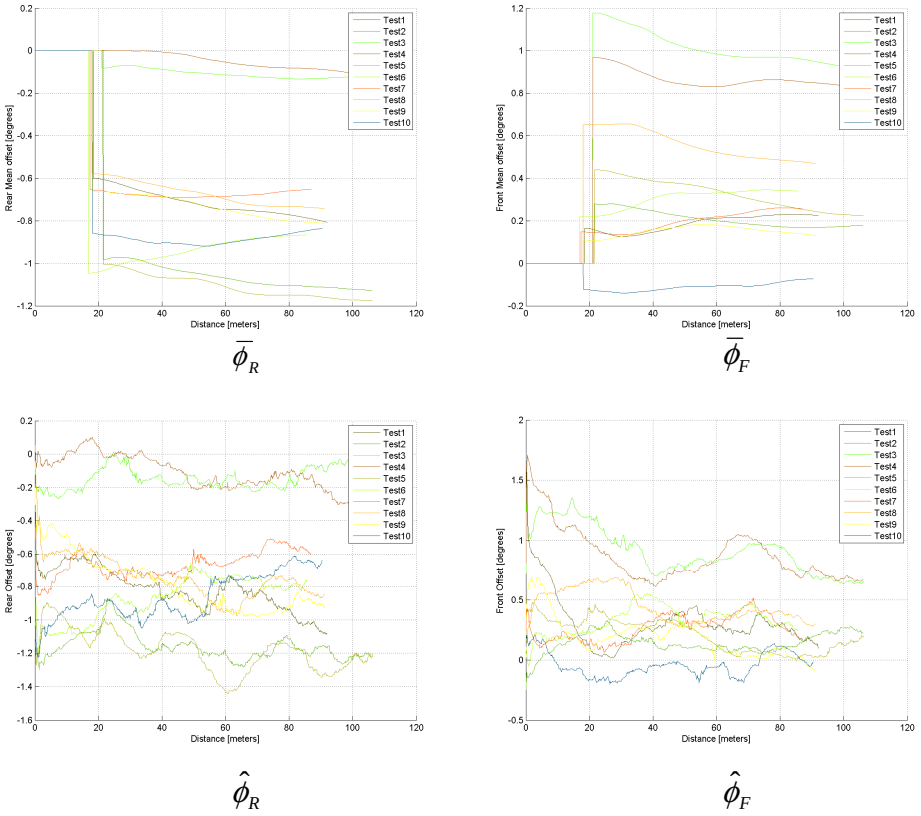

Figure 11: Angular offsets estimated from 10 different data sets recorded along straight paths in Kemi.

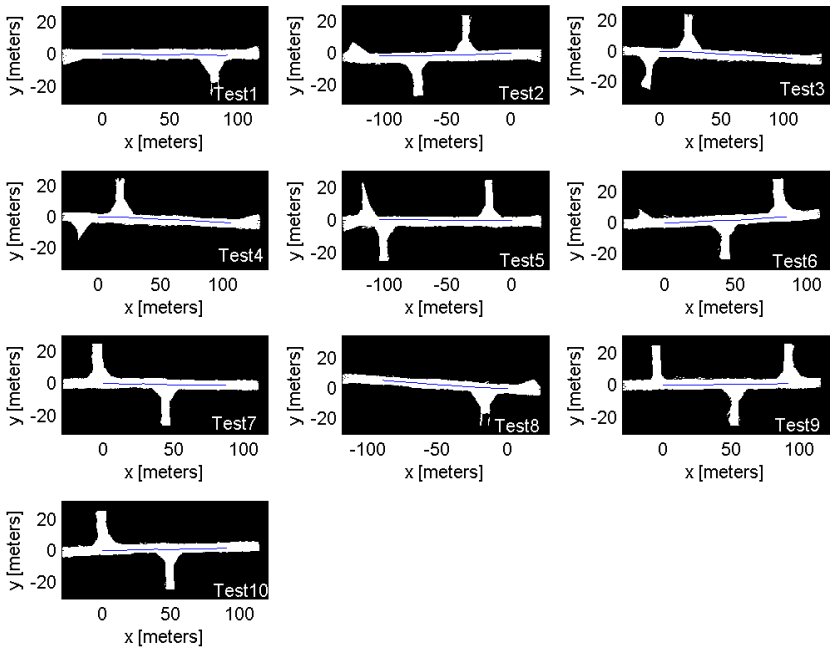

Figure 12: Maps and paths, in blue, from the straight areas in Kemi. The paths starts in position (0,0) m with heading equal to 0^o.

In Figure 11 $\bar{\phi}_R$, $\bar{\phi}_F$, $\hat{\phi}_R$ and $\hat{\phi}_F$ can be seen from data recorded along real straight paths in Kemi, see maps in Figure 12. From looking at the figure it can be seen that the offsets are spread around (ϕ_R, ϕ_F) equal to (-0.8; 0.3)^o, which is the true offset. 8 of the 10 final $(\bar{\phi}_R, \bar{\phi}_F)$:s are inside the ±0.5^o limit and the same 8 are inside the limits after only 23 m. By looking at $(\hat{\phi}_R, \hat{\phi}_F)$ it can be seen that some estimates converge fast and some takes longer time, especially for $\hat{\phi}_F$. All of them have converged close to their final value after 40 m and $(\bar{\phi}_R, \bar{\phi}_F)$ have get close to their final values after around 50 m. The computation time was around 17 minutes in all cases.

7.2.2 Turning in a normal mine drift

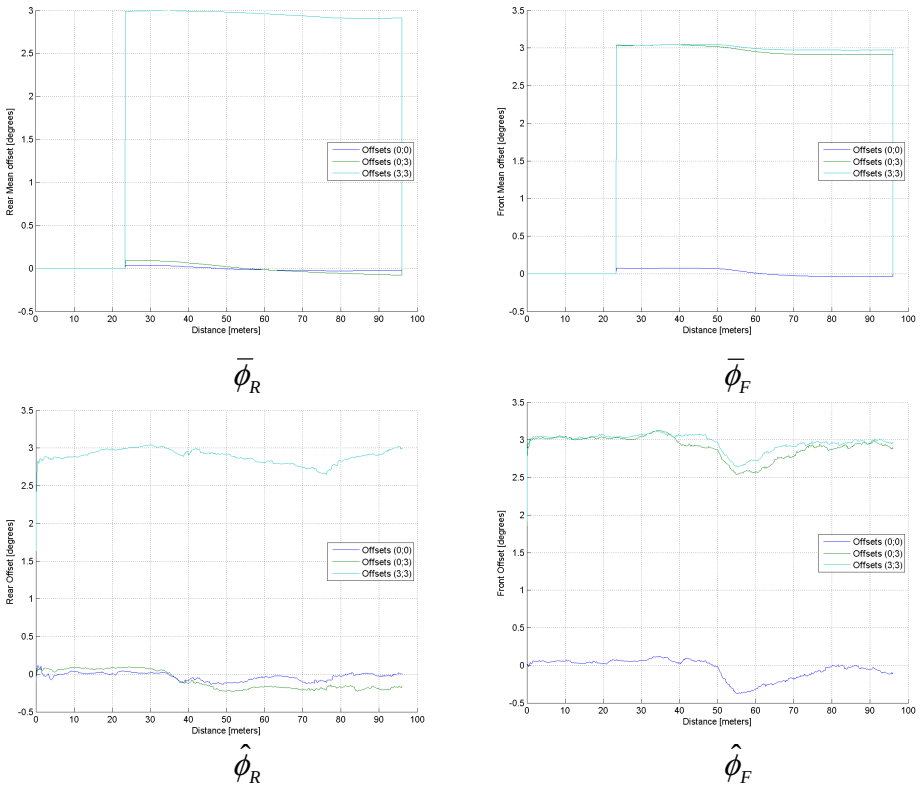

$\bar{\phi}_R$ $\bar{\phi}_F$

$\hat{\phi}_R$ $\hat{\phi}_F$

Figure 12: Angular offsets estimated from a simulated route in Kemi with a turn and laser offsets {(0,0) (0,3) (3,3)}^{o}. As seen, $\hat{\phi}_F$ get affected at the turn after 55 meters.

Figure 12 shows $\bar{\phi}_R$, $\bar{\phi}_F$, $\hat{\phi}_R$ and $\hat{\phi}_F$ when simulating with the offsets {(0,0) (0,3) (3,3)}^{o}. The offsets have converged to within ±0.1^o when the mean valuing is started after 23 m and doesn't get largely affected by the turn after 50 m. As seen by $(\hat{\phi}_R, \hat{\phi}_F)$ the offsets converge after a few meters. $\hat{\phi}_F$ does get affect in the turn but then returns to its original value. For $\hat{\phi}_R$ it's hard to see if it is affected by the turn. Its largest reaction happens after 70 m, which is when the back has left the turn and is facing towards it.

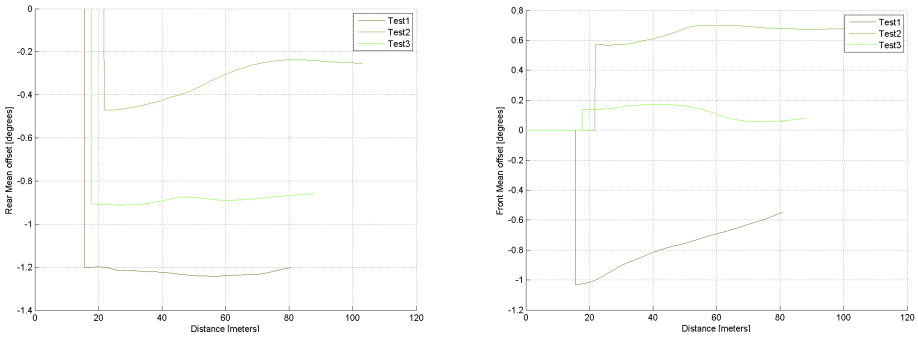

$\bar{\phi}_R$

$\bar{\phi}_F$

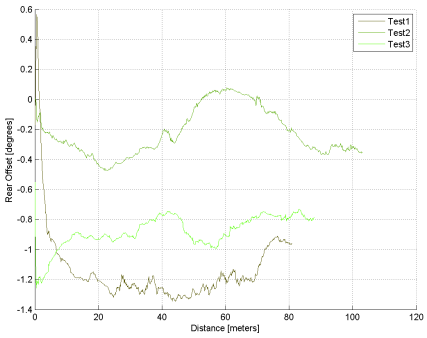

$\hat{\phi}_R$

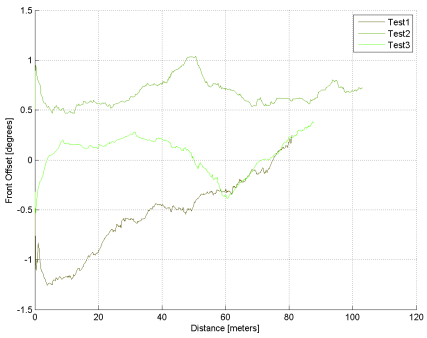

$\hat{\phi}_F$

Figure 13: Angular offsets estimated from real data recorded along a path including a turn.

The same accuracy was not achieved when using real data in real turning cases. This can be seen in Figure 13 showing $\bar{\phi}_R$, $\bar{\phi}_F$, $\hat{\phi}_R$ and $\hat{\phi}_F$ when driving the routes seen in Figure 14, starting at (0,0) m with heading 0^o. Test 3 is the only case when both offsets are within the $\pm 0.5^o$ limit and close to the true offsets. Test 2 is on the border of the $\pm 0.5^o$ range with $\bar{\phi}_F$ and close but outside with $\bar{\phi}_R$. In test 1 only $\bar{\phi}_R$ is in the range but by looking at $\hat{\phi}_F$ in Figure 13, it's seen that $\hat{\phi}_F$ after the turn, seen in Figure 14, converges towards the true offset. It could also be seen that $\hat{\phi}_F$ in test 3 deviates at the turn after 60 m and then returns. In test 2 the offset is deviating all the time from the true but especially when the turn is made. The computation time is around 15 minutes.

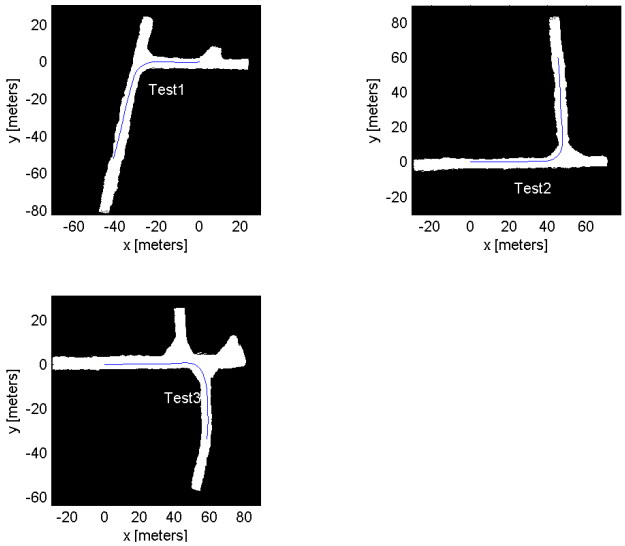

Figure 14: Maps and paths, in blue, from 3 areas with a turn in Kemi. The paths begins at position (0,0) m with heading 0^{o}.

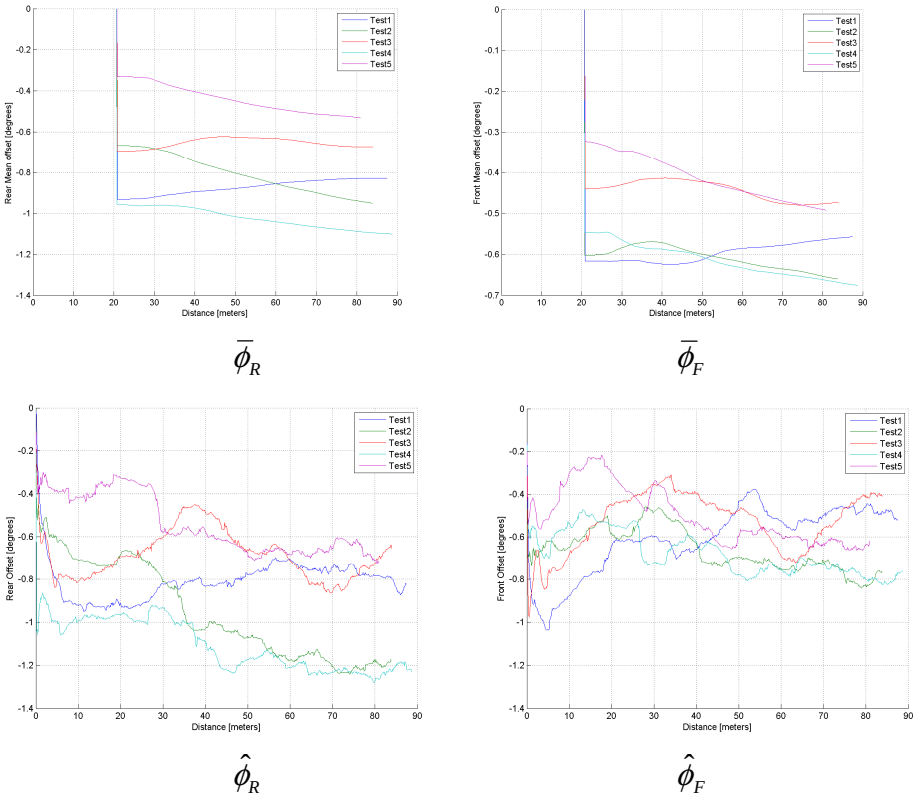

$\bar{\phi}_R$ $\bar{\phi}_F$

$\hat{\phi}_R$ $\hat{\phi}_F$

Figure 15: Angular offsets estimated from 5 real routes in Kvarntorp.

7.2.3 Driving in a straight wide mine drift

Simulations from Kvarntorp gave offsets ($\bar{\phi}_R, \bar{\phi}_F$) within ±0.2° of the true offsets. The simulations also showed that the effects of the small turns in the end are neglect able.

Figure 15 shows $\bar{\phi}_R$, $\bar{\phi}_F$, $\hat{\phi}_R$ and $\hat{\phi}_F$ estimated from data recorded in Kvarntorp. For all the Kvarntorp runs the offsets are the same but not known and it's hard by just looking at Figure 15 to see what the true offsets could be because of the large spread. The worst ones are the rear offsets which are spread ±0.25° at all times. Even though it's hard to see the true offsets it can be seen in Figure 15 that ($\bar{\phi}_R, \bar{\phi}_F$) are inside the ±0.5° limit after 23 meters if the true offsets are somewhere between the estimated ones. The computation time is around 20 minutes.

From looking at ($\hat{\phi}_R, \hat{\phi}_F$) in Figure 15 it could be seen that for both offsets test 1, 3 and 5 are grouped together and similar with test 2 and 4. Figure 16 shows the driven paths super imposed on maps of the environment. All paths begin in position (0,0) m with heading 0°. In tests 1, 3 and 5 the machine was driving forward, while 2 and 4 are recorded while driving backwards. It's thereby a correlation between the direction and especially the rear offsets. From Figure 15 it can be seen that it takes 50 m for ($\hat{\phi}_R, \hat{\phi}_F$) to stabilize and because the paths are not longer than 80 m ($\bar{\phi}_R, \bar{\phi}_F$) do not have time to stabilize at the final value. The noise on the maps in Figure 16 is because of holes in the wall into a side drift.

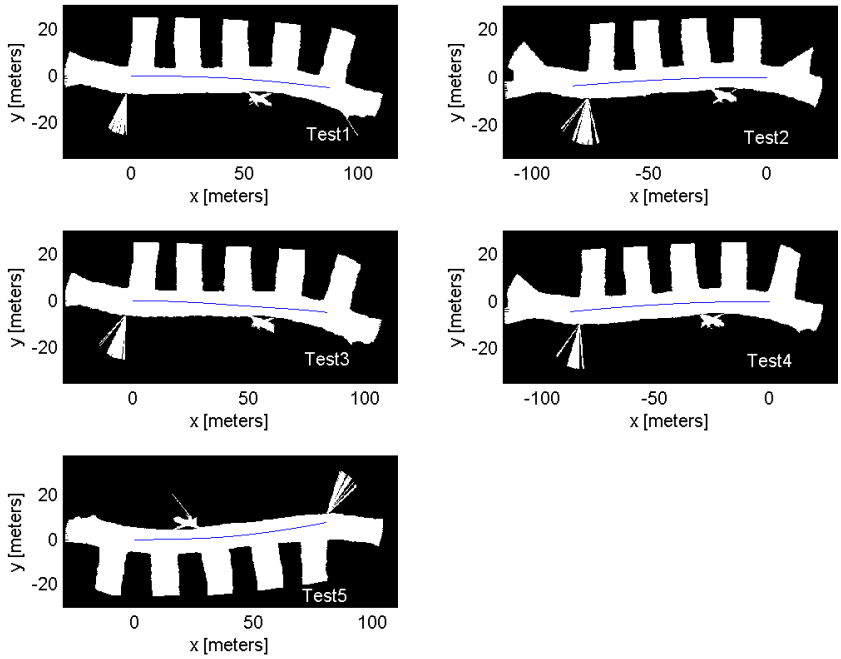

Figure 16: The 5 maps and paths, in blue, from Kvarntorp. The paths begins at position (0,0) m with heading 0°.

7.3 Discussion

In Chapter 6 it was found that an accuracy of $\pm 0.5^o$ was needed to get a scan matching error less than 0.35. It's here seen that it's possible in most cases to achieve this accuracy after only 23 m if the machine is going straight. Possibly it could have been achieved faster if the mean valuing had started earlier since the offsets ($\hat{\phi}_R, \hat{\phi}_F$), according to Figure 11, in most cases have converged after only a few meters. The computation time is also less than the required 30 minutes.

The reason for tests 3 and 4 in Figure 11 to lie outside the allowed range can't be properly explained. Tests 1 and 8 are made in the same drift and in test 1 there are only minor problems to converge in the beginning. In test 8 there are larger problems in the beginning and the start position is in the same place as in tests 3 and 4. It may be that the machine is starting in a junction, resulting in the estimated offsets getting stuck in local minima.

It could also be observed that the wall is noisy after half the path. This may also be the reason why tests 3 and 4 don't converge after the junction. Investigations of ε_{match} have shown that it decreases for tests 3 and 4 compared to in test 8 at the place of the noisy wall, which strengthens the theory. This happens because the noisy wall changes the optimal point searched for by the Kalman filter. The noise may come from a cable ladder or ventilation drum. What is causing the constant offsets between the tests in the same areas has yet to be proven. Probably it has to do with differences in the starting point, steering of the machine, noise in the gyro and so on.

A probable reason for ($\hat{\phi}_R, \hat{\phi}_F$) to deviate from their true offsets in the simulated and real turns in Figure 12 and Figure 13 is because of geometry of the turn, as mentioned in Chapter 6.3. The theory is strengthen by the fact that $\hat{\phi}_R$ in one of the simulated cases isn't affected until after the turn, and that we don't have simulated odometry errors. Test 2:s behaviour, seen in Figure 13, can't be explained. Something makes the offset deviate even on the straight parts.

Later examination of the machine used at data collection in Kvarntorp showed that a part in the hinge angle sensor was broken. This gave the hinge angle sensor a play. The load on the hinge angle changes when the machine goes in different directions, which then probably affected its readings because of the play. This is probably the reason for the grouping in the tests seen in Figure 15. Positioning of the rear part of the machine depends directly on the hinge angle, which can be the reason for the rear offsets to get more affected.

The algorithm works in all simulated cases which mean that it is theoretically correct. More experiments in a controlled environment are needed to draw some definitive conclusions for the real cases but from the experiments made it can be concluded that the offsets in most cases can be estimated to within $\pm 0.5^o$, if the environment doesn't contain too much disturbance. The requirements are

that the machine is driven straight for at least 23 m at a speed of around 2.5 m/s. It even seems to work in wide drifts with side drifts. The computation time increases with the width of the drift but stays below 30 minutes.

8 Conclusion

This report presents two methods that have been developed for use in calibration of the hinge angle sensor respectively the two laser scanners on an Atlas Copco ST14 LHD. In both the hinge angle calibration and laser scanner calibration the new methods finds the angular offset of the sensors.

For hinge angle calibration we have developed an algorithm based on the difference between the measured hinge angle value and the expected value modelled from the speed and the heading change as measured by the gyro. In the laser scanner calibration we used state augmentation together with an already existing Kalman Filter to estimate the angular offsets of the laser. A SLAM algorithm was also implemented to solve the problem with cross dependence between the map and the offsets at the calibration.

Both methods satisfy the predefined criterions that no surrounding equipment should be needed and no extra sensors should be needed. They also satisfy the requirement of easy operation. The operator only needs to drive approximately straight for around 50 meters while recording data and then supply the calibration program with the log-file. Both methods can also operate offline and deliver estimates in under 30 minutes as requested.

To test accuracy and dependence on outer parameters a number of experiments and tests were made with both methods. The dependence on speed, distance and steering angle was analytically investigated for the hinge angle calibration to get the characteristics of the system. Real experiments were then made to confirm the characteristics and find the limits of the system. For the laser scanners the required precision was only known as a maximum scan matching error in the map and not as a sensor offset. An investigation was therefore first made to find the offsets that gave the maximum scan matching error. The system was to complex to do analytical investigations, instead simulations and real tests were made to test the accuracy of the system and how long driving distance and time that was needed to do the estimation. The tests were made in normally sized tunnels, tunnels with a turn and wide tunnels with side drifts to test how the method handle different environments.

The experiments showed that the hinge angle calibration method is only able to deliver accurate estimates two within $\pm 0.3^{o}$ in 33 m or more. It is also required that the machine drive straight for this to be achievable. The tests showed that the laser calibration method is able to deliver the required accuracy of $\pm 0.5^{o}$ in around 15 minutes, and that a distance of 23 m in most cases is sufficient if the machine is driven straight. Problems arise if there are to much environmental disturbance or if the machine makes large turns. For both methods a speed of 2.5 m/s is recommended.

The laser calibration method and the hinge angle method both need further evaluation in the future. More experiments needs to be done to better establish the confidence interval of both methods. As explained above side drifts interfere the laser offsets estimation and maybe also the positioning so it needs to be investigated further.

In Atlas Copco auto traming system maps are today created using only odometry. In the future one could use the maps from the laser calibration method instead where the positioning is made using both odometry and laser measurements. One could also augment the hinge angle sensor offset to the states and use the laser calibration method for the hinge angle offset estimation. The hinge angle method could also be run online, when the offset is known to keep track of the gyro and hinge angle sensor to see if an error occur, because then the method deliver a different value compared to the true offset.

Finally the developed methods considerably simplify the calibration of the three sensors compared to the methods used before. Both methods delivered such a good results that Atlas Copco choose to implement them in their system.

9 References

Altafini, C. (1999). A path-tracking criterion for and LHD articulated vechicle. *International Journal of Robotics Research*, Vol. 18, No. 5, pp. 435-441. May 1999.

AutoMine (2011). Available: http://www.miningandconstruction.sandvik.com. [2011-02-02]

Borenstein, J. (1996). Measurements and Correction of Systematic Odometry Errors in Mobile Robots. *IEEE Transactions on robotics and automation*. vol. 12, No. 6, pp. 869-880. December 1996.

Dall Larsen, T., Bak, M., A. Andersen, N. & Ravn O. (1998). Location Estimation for and Autonomously Guided Vehicle using and Augmented Kalman Filter to Autocalibrate the Odometry. *IEEE International Conference* FUSION. (pp. 245-250). Las Vegas, Nevada, USA 6-9 July 1998.

De Ceccco, M. (2002). Self-Calibration of AGV Inertial-Odometric Navigation Using Absolute-Reference Measurements. *IEEE Instrumentation and Measurement Technology Conference*. (pp. 1513-1518). Anchorage, Alaska, USA 21-23 May 2002.

Hainsworth, D.W (2001). Teleoperation User Interfaces for Mining Robotics. *Autonomous robots*, vol. 11, ss. 19-28.

Larsson, J., Broxvall, M. & Saffiotti, A. (2010). An evaluation of local autonomy applied to teleoperated vehicles in underground mines. *IEEE International Conference on* Robotics and Automation (ICRA) (pp. 1745-1752). Anchorage, Alaska, USA 3-8 May 2010.

Madhavan, R., Dissanayake, M.W.M.G. & Durrant-Whytel, H.F. (1998). Autonomous Underground Navigation of an LHD using a Combined ICP-EKF

Approach. *IEEE International Conference on* Robotics and Automation (ICRA) (pp. 3703-3708) Leuven, Belgium May 1998.

Marshall, J., Barfoot, T., & Larsson, J. (2008). Autonomous Underground Tramming for Center-Articulated Vehicles. *Journal of Filed Robotics,* Vol. 25, Issue. 6-7, pp. 400-421. June 2008.

Martinelli, A., Tomatis, N., Tapus, T. & Siegwart, R. (2003). Simultaneous Localization and Odometry Calibration for Mobile Robot. *IEEE/RSJ International Conference on* Robots and Systems (pp. 1499-1504). Las Vegas, Nevada, USA October 2003.

Martinez-Cantin, R. & A. Castellanos, J (2005). Unscented SLAM for large-scale outdoor environments. *IEEE/RSJ International Conference on Intelligent Robots and Systems (IROS)*. (pp. 3427-3432). Edmonton, Alberta, Canada 2-6 August 2005

Merwe R., Doucet, A., Freitas, N. & Wan, E. (2000). *The unscented particle filter,* Cambridge Univ., Eng. Dep., Cambridge, U.K., Tech. Rep. CUED/F-INFENG/TR 380. 2000.

MINEGEM (2011). Available: http://www.cat.com. [2011-02-02]

Ridely, P. & Corke, P. (2001). Autonomous Control of an Underground Mining Vehicle. *Australian Conference on Robotics and Automation*. (pp. 27-31). Sydney, Australia 14-15 November 2001.

Scooptram Automation (2011). Available: http://www.atlascopco.com. [2011-02-02]

Simon, D. (2006). *Optimal State Estimation: Kalman, H Infinity, and Nonlinear Approaches*. Hoboken: John Wiley & Sons

10 Appendix A

10.1 Only using hinge angle measurements

One idea was to use the mean of all recorded hinge angle offsets, while driving in an almost straight mine, where one could see all the way. The maximum error occurs if one drives in an arc with width equal to two times the tunnel width and reaching from one end to the other. With a 5 m wide tunnel calculations using Eq. (1) combined with formulas for a circular segment showed that 203 m was needed to get a precision of 0.2^{o}. The problem is that 200 m long tunnel ways are rare.

Another idea used the fact that if you drive in a tunnel in one direction and accumulate the angles then turn the machine around and drive the same way back while still accumulating. The mean of the accumulated angle is the offset. This solution had the problems that one need to turn the machine around and also drive exactly the same way back and get the same slip in the mine drift intersections to make it work. This ended up with the last alternative using the gyro.

10.2 Gyro ideas

A number of ideas were put-up how to estimate the hinge angle offset γ_o using the gyro and the odometer information. Both the hinge angle sensor and the gyro give the same information. For example suppose the hinge angle γ is small and $\dot{\gamma}$ is equal to zero. Then Eq. (1) can be simplified to

$$\dot{\theta}_1 = \frac{v\gamma}{l_2 + l_1}.$$

It shows that the rotation speed $\dot{\theta}_1$ given by the gyro is only a scaling by speed of the hinge angle. At $\dot{\theta}_1$ equal to zero the hinge angle sensor should give zero γ.

A method was wanted that found $\gamma_m(n)$ in the point where $\dot{\theta}_1$ is equal to zero because then $\gamma_m(n)$ only contains γ_o and noise according to Eq. (4). One method was to drive straight with the mean of $\hat{\dot{\theta}}_{ubm}(n)$ equal to zero and then calculate the mean of the measured $\gamma_m(n)$, which should then only include the offset. This was thought to be too hard for the driver. Another method was to interpolate a line between two $\hat{\dot{\theta}}_{ubm}(n)$ samples with opposite signs and two $\gamma_m(n)$ samples at the same time instants. Then use the proportional distance between the first $\hat{\dot{\theta}}_{ubm}(n)$ and zero on the $\hat{\dot{\theta}}_{ubm}$-line to find γ_o on the γ_m-line and taking the mean from many interpolations to find the true γ_o. A third and final idea was to use Eq. (1) together with system identification and then insert the measured $\gamma_m(n)$ to find a γ_o that gives the best fit with the measured $\hat{\dot{\theta}}_{ubm}(n)$. This required an optimization algorithm. By analysing this idea further it was found out, as seen in Chapter 3.3.1, that γ_o could be found explicit.

11 Appendix B

Two plots were created for each experiment setup. The first shows data from using gear 1 and 2 and the second shows data from using gear 2 and 3. In the plots the estimated offsets $\hat{\gamma}_o$(p) for each experiment can be seen as a circle and their individual 99 % confidence intervals $z_{0.99}\sigma_{\hat{\gamma}_o 1}(p)$ be seen as bars. The dashed doted lines show the mean hinge angle offset $\bar{\hat{\gamma}}_o$ for each gear. Dashed lines indicate the estimated 99 % confidence interval $z_{0.99}s_{\hat{\gamma}_o}$ for the true offset γ_o, calculated from the spread of the offsets $\hat{\gamma}_o$(p) for each gear. The coloured areas shows the 99 % confidence interval, defined by $z_{0.99}L_1$ and $z_{0.99}L_2$, for the true 99 % confidence interval of γ_o.

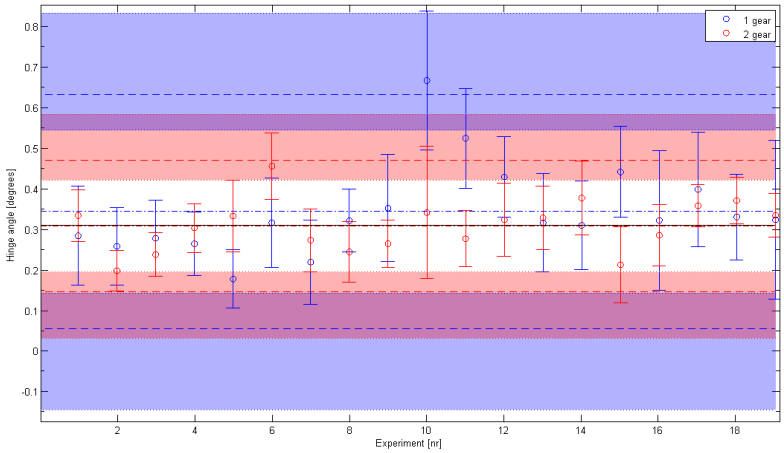

Figure 17: 19 estimated offsets when using 250 samples and driving straight with gear 1 and 2.

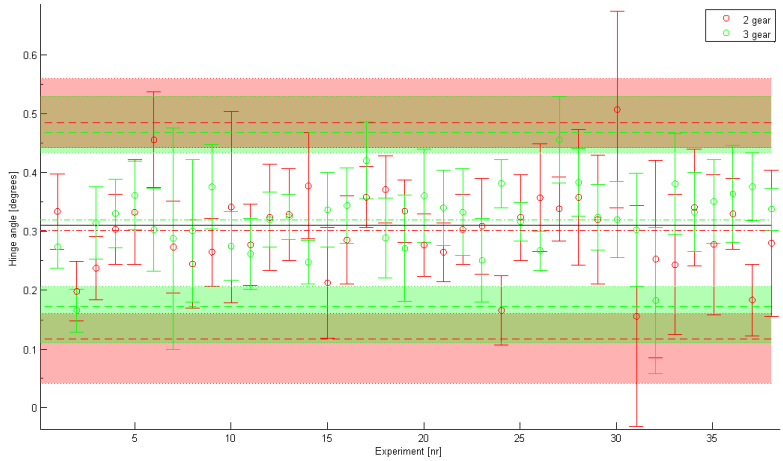

Figure 18: 38 estimated offsets when using 250 samples and driving straight with gear 2 and 3.

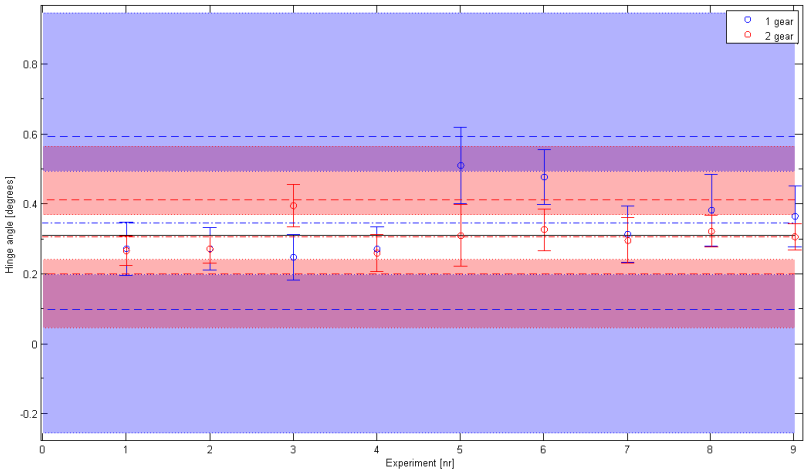

Figure 19: 9 estimated offsets when using 500 samples and driving straight with gear 1 and 2.

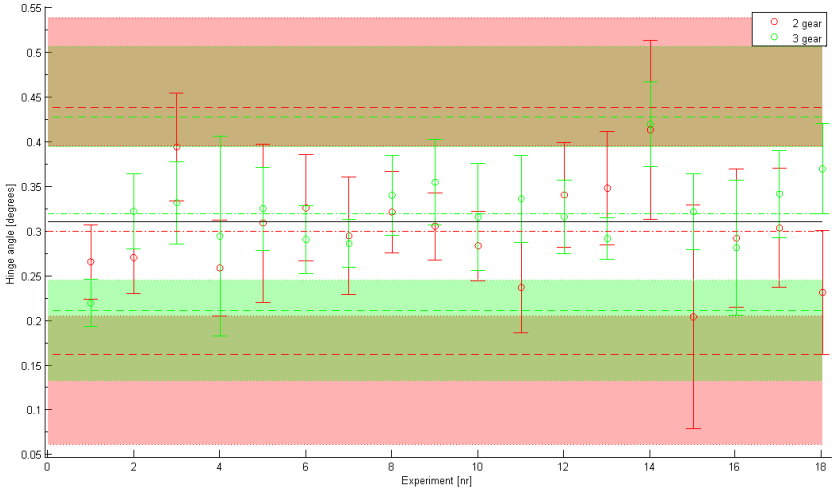

Figure 20: 18 estimated offsets when using 500 samples and driving straight with gear 2 and 3.

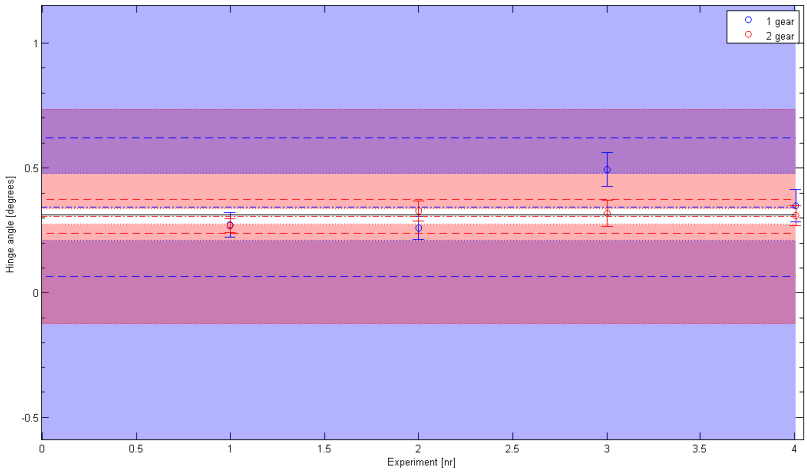

Figure 21: 4 estimated offsets when using 1000 samples and driving straight with gear 1 and 2.

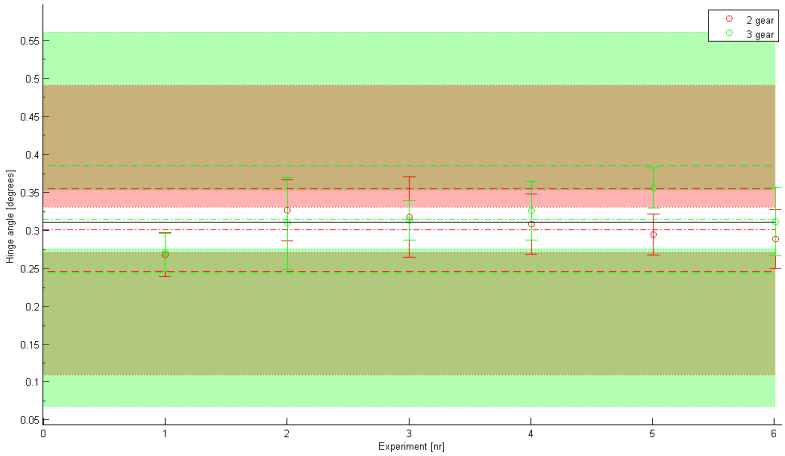

Figure 22: 6 estimated offsets when using 1000 samples and driving straight with gear 2 and 3.

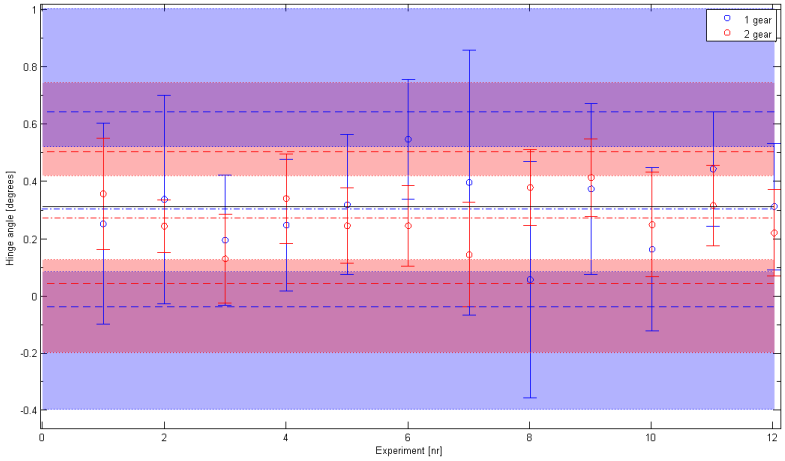

Figure 23: 12 estimated offsets when using 250 samples and driving with a true hinge angle of 0.2^{o} using gear 1 and 2.

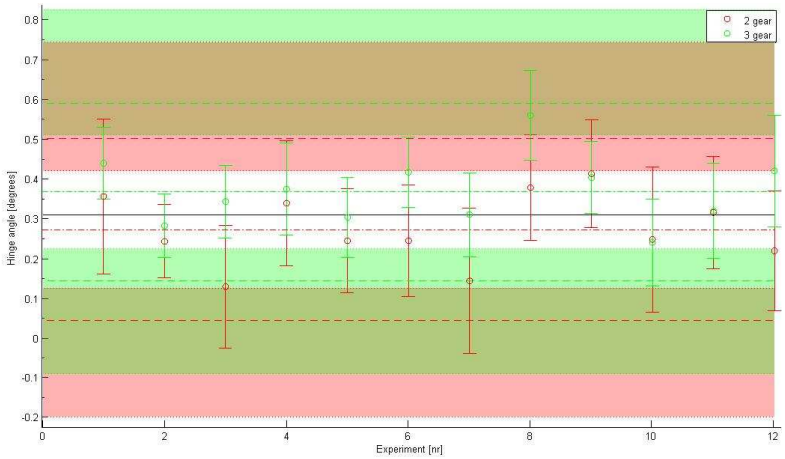

Figure 24: 12 estimated offsets when using 250 samples and driving with a true hinge angle of 0.2^{o} using gear 2 and 3.

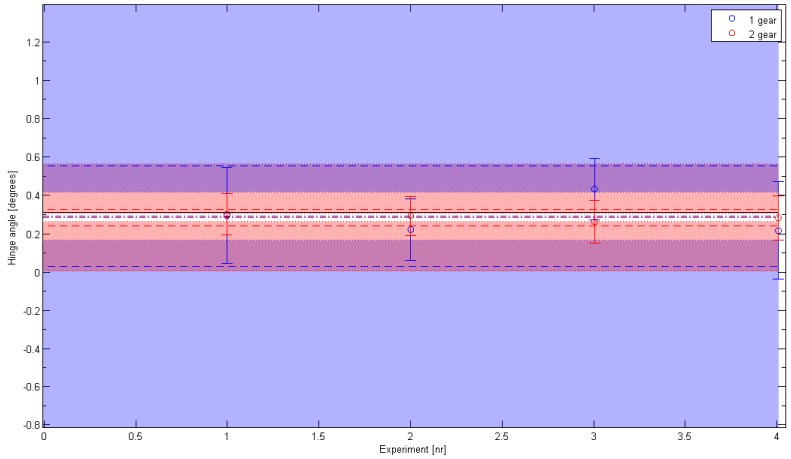

Figure 25: 4 estimated offsets when using 500 samples and driving with a true hinge angle of 0.2^{o} using gear 1 and 2.

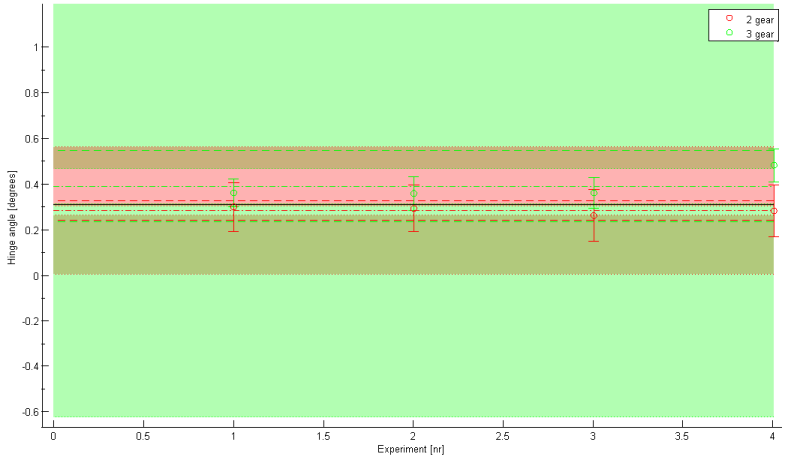

Figure 26: 4 estimated offsets when using 500 samples and driving with a true hinge angle of 0.2^{o} using gear 2 and 3.

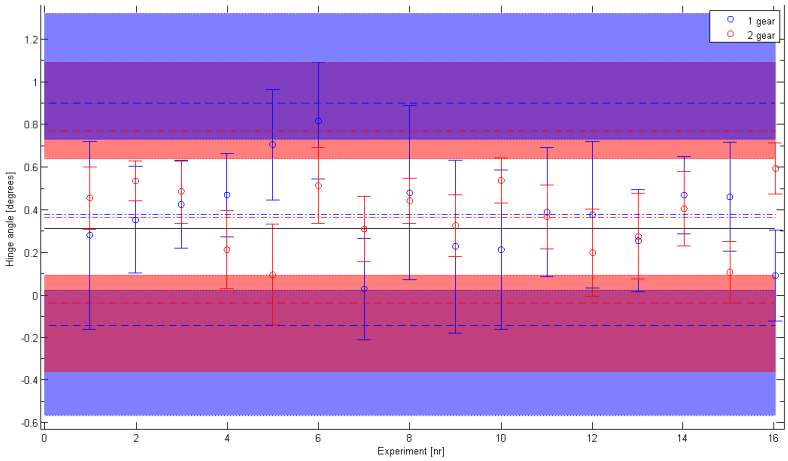

Figure 27: 16 estimated offsets when using 250 samples and driving with a true hinge angle of $+0.7^{o}$ using gear 1 and 2.

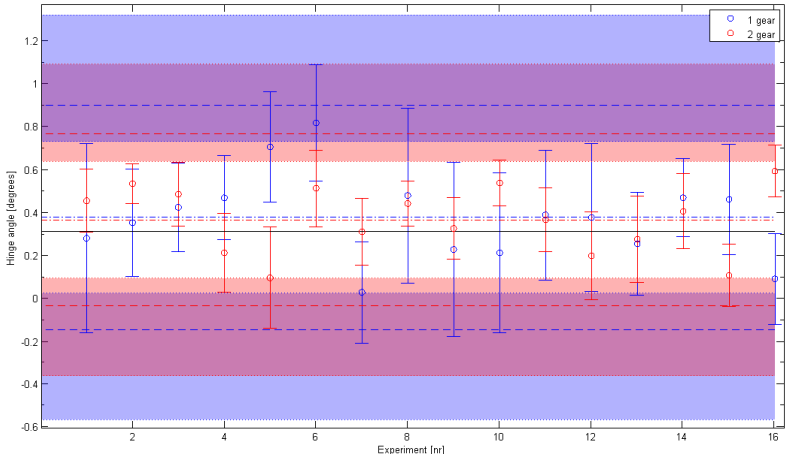

Figure 28: 16 estimated offsets when using 500 samples and driving with a true hinge angle of $+0.7^{o}$ using gear 1 and 2.

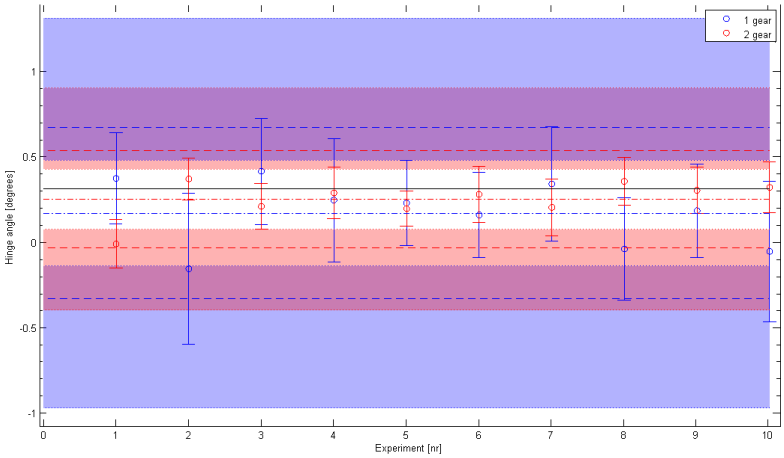

Figure 29: 10 estimated offsets when using 250 samples and driving with a true hinge angle of -0.7^{o} using gear 1 and 2.

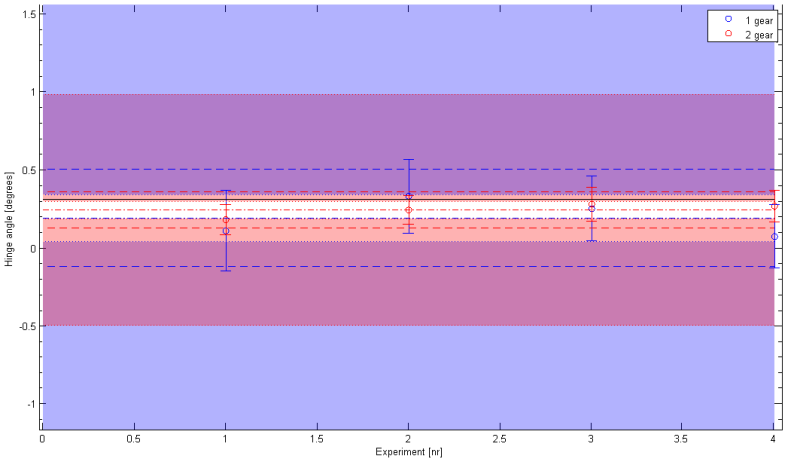

Figure 30: 4 estimated offsets when using 500 samples and driving with a true hinge angle of -0.7^{o} using gear 1 and 2.